nature biomedical engineering

Article

https://doi.org/10.1038/s41551-026-01614-w

DNA origami vaccine nanoparticles improve humoral and cellular immune responses to infectious diseases

Received: 29 December 2023

Accepted: 13 January 2026

Published online: 11 March 2026

Check for updates

Yang C. Zeng[1,2,3,12] ✉, Olivia J. Young[2,3,4,12], Qiancheng Xiong[1,2,3,12], Longlong Si[2,12], Min Wen Ku[2,12], Sylvie G. Bernier[2], Hawa Dembele[1,2,3,5], Giorgia Isinelli[1,2], Tal Gilboa[2,6], Zoe Swank[2,6], Su Hyun Seok[1,2,3,7], Anjali Rajwar[2], Amanda Jiang[2], Yunhao Zhai[2], LaTonya D. Williams[8], Caleb A. Hellman[8], Chris M. Wintersinger[1,3], Amanda R. Graveline[2], Andyna Vernet[2], Melinda Sanchez[2], Sarai Bardales[2], Georgia D. Tomaras[8], Ju Hee Ryu[1,7,9], Ick Chan Kwon[1,7,9], Girija Goyal[2] ✉, Donald E. Ingber[2,10,11] ✉ & William M. Shih[1,2,3] ✉

Current SARS-CoV-2 (severe acute respiratory syndrome coronavirus 2) vaccines have shown robust induction of neutralizing antibodies and $CD4^+$ T cell activation; however, $CD8^+$ responses are variable, and the duration of immunity and protection against variants are limited. Here we repurpose our DNA origami vaccine nanotechnology DoriVac to target infectious viruses, namely, SARS-CoV-2, HIV and Ebola. The DNA origami nanoparticle, conjugated with infectious-disease-specific heptad repeat 2 peptides, which act as highly conserved antigens, and CpG adjuvant at precise nanoscale spacing, induces neutralizing antibodies, Th1 $CD4^+$ T cells and $CD8^+$ T cells in naive mice, with significant improvement over a bolus control. Pre-clinical studies using lymph-node-on-a-chip systems validate that DoriVac, when conjugated with antigenic peptides or proteins, induces promising cellular and humoral immune responses in human cells. Moreover, DoriVac bearing full-length SARS-CoV-2 spike protein achieves immune responses comparable to current mRNA vaccine platforms while potentially reducing storage constraints. These results suggest that DoriVac holds potential as a versatile, modular vaccine platform, capable of inducing both humoral and cellular immunities, underscoring its potential future use.

Initial focus on rapid vaccine design for pandemics[1–5] led to the novel messenger RNA vaccines, mRNA-1273 (manufactured by Moderna) and BNT162b2 (manufactured by Pfizer), which rely on lipid nanoparticle (LNP) delivery of mRNA encoding an early variant of the spike protein. Despite their success, the emergence of SARS-CoV-2 (severe acute respiratory syndrome coronavirus 2) variants like B.1.351 (Beta)[6], B.1.617.2 (Delta)[7] and B.1.529 (Omicron)[8] raised concerns about the vaccine efficacy as variants showed the ability to evade immunity[9–15]. The immune evasion observed with current vaccines necessitates interventions effective against mutations.

Current SARS-CoV-2 vaccines focus on the receptor binding domain (RBD) of the spike protein. Viruses rely on RBD to bind to cells and initiate infection and then heptad repeat 1 (HR1) and heptad repeat 2 (HR2) to fuse the viral and cell membranes. HR1 and HR2, conserved across various viruses, self-assemble into α-helical coils and then assemble into superhelical structures to facilitate fusion[16–21].

A full list of affiliations appears at the end of the paper. ✉e-mail: yang_zeng@dfci.harvard.edu; girija.goyal@wyss.harvard.edu; don.ingber@wyss.harvard.edu; william_shih@dfci.harvard.edu

While the RBD region and other viral regions are subject to viral evolution, HR1 and HR2 sequences remain highly conserved, providing a conserved antigen for vaccines[22]. Only three amino acids differ between the original SARS-CoV-2 HR2 sequence and the Omicron variant (Supplementary Table 1). HR1 and HR2 also harbour T cell epitopes and may induce neutralizing antibodies, serving as viable antigens for vaccine design[23,24]. HR2, with a simpler structure than HR1, has been successfully targeted by vaccines[22,25] and was selected as the antigen for delivery via our vaccine nanotechnology for SARS-CoV-2, human immunodeficiency virus (HIV), and Ebola (Supplementary Table 2).

While the vaccine community traditionally prioritized neutralizing antibody responses[26], there is now growing acknowledgement of the essential role of cellular immune responses (dendritic cells (DCs), cluster of differentiation 4-positive ($CD4^+$) and cluster of differentiation 8-positive ($CD8^+$) T cells) for broad viral protection[9,24,27–33]. Functional T cells prevent immune escape of mutated strains[9]. SARS-CoV-2 mutated strains have been demonstrated to escape neutralizing antibody responses, but not T cell responses[34]. $CD4^+$ T cells support antibody generation[35], and studies show that $CD4^+$ T cell transfer can protect against viral challenge[36]. Mild SARS-CoV-2 infections exhibit robust $CD8^+$ T cell reactivity[37,38] contributing to rapid viral clearance[29]. Depleting $CD8^+$ T cells in non-human primates increases susceptibility to SARS-CoV-2 re-infection[39]. In HIV and Ebola, $CD8^+$ T cells are crucial for long-term control and vaccine-induced protection. $CD8^+$ depletion led to failure in controlling simian immunodeficiency virus in non-human primates[40,41]. In Ebola, $CD8^+$ cells were essential for immune protection in non-human primates, while antibody transfer failed to protect[42]. An ideal vaccine should induce both humoral and cellular immune responses, including neutralizing antibodies and long-term memory T cells[9]. mRNA vaccines show robust $CD4^+$ responses but variable $CD8^+$ responses; both influence long-term immunity[43–47].

Multiple vaccine candidates have been developed to induce neutralizing antibodies and cellular responses against the SARS-CoV-2 spike protein, including over 60 different nanoparticle formulations[48,49]. Despite the success of LNP-based mRNA vaccines, these vaccines face challenges like manufacturing complexity, cold-chain requirements, limited stability, high cost, poor cargo loading efficiency, limited control over cargo stoichiometry, and off-target effects[48,50]. In this Article, we introduce DoriVac, a DNA origami vaccine nanoparticle, as a versatile nanotechnology for infectious diseases. While previous studies have demonstrated vaccine delivery with DNA origami for cancer[51–54] and individual infectious diseases[55–58], this study aims to demonstrate its broad applicability for infectious diseases. DoriVac induced robust humoral and T cell immune responses against SARS-CoV-2, HIV and Ebola viruses in mouse models, demonstrating the nanotechnology's programmability for various infectious-disease HR2 antigens. This approach may broadly apply to pathogen vaccine development by conjugating the respective antigens to the DNA origami. Our current study also includes a full-length spike protein conjugation strategy that elicited immune responses comparable to state-of-the-art mRNA-based SARS-CoV-2 vaccines, generating rapid early antibody responses after one dose, further highlighting DoriVac's promise as a next-generation, broadly applicable vaccine platform.

Fabrication of modular DoriVac nanoparticles

We previously developed a DNA origami nanoparticle, termed square block (SQB) for its square-lattice architecture for precise spatial presentation of cytosine–phosphate–guanine (CpG) adjuvants[52]. Formed through self-assembly of a long scaffold strand with corresponding short 'staple' strands, DoriVac is easy to manufacture and highly stable without cold-chain requirements, exhibits high occupancy of designed cargo-binding sites due to the robustness of DNA hybridization and offers precise control over cargo attachment. This nanotechnology facilitates optimized spatial arrangement of immune-activating adjuvants, resulting in robust cellular immune responses in various cancers, as previously published[52]. The SQB flat face, modified with 18 CpG strands at 3.5 nm spacing, induces type I (Th1) skewed immune activation (Fig. 1a)[52].

We applied DoriVac technology to create vaccines for SARS-CoV-2, HIV and Ebola viruses by linking highly conserved viral HR2 peptides to the extruding face of the SQB nanoparticles (Fig. 1a). HR2 peptides contain major histocompatibility complex (MHC) class I (MHC-I) and class II (MHC-II) epitopes, which are crucial for broadly activating cellular immunity. To this end, we designed peptide–oligonucleotide conjugates with the appropriate 'anti-handle' strand through dibenzocyclooctyne (DBCO)-azide click chemistry for specific attachment onto 24 specific 'handle' sites of the extruding face of the SQB (Fig. 1a,b). The SQB nanoparticle co-delivers CpG adjuvant and disease-specific HR2 antigens to antigen presenting cells. The CpG sequence used in DoriVac remains unchanged from our previous studies, where it was shown to induce robust Th1-skewed immune activation in mouse models[52]. B cells produce neutralizing antibodies, which can block the membrane fusion of the virus with the host cell (Fig. 1c). DCs present and cross-present the antigens to activate both $CD4^+$ and $CD8^+$ T cells (Fig. 1d). The oligonucleotide–HR2–peptide conjugates were purified via polyacrylamide gel electrophoresis (PAGE) purification (Fig. 1e). The agarose-gel electrophoresis band shift shows successful fabrication of peptide-functionalized SQB (Fig. 1f). To confirm peptide conjugation efficiency to the SQB, we digested the DNA origami via DNase I and estimated peptide occupancy of greater than 95% of the conjugation sites via silver stain (Fig. 1g,h and Supplementary Table 3). Fabrication of SARS-CoV-2-HR2, HIV-HR2 and Ebola-HR2 DoriVac was verified via transmission electron microscopy (TEM) (Fig. 1i–l and Supplementary Fig. 1). Aggregation was observed via agarose gel,

Fig. 1 | DNA origami vaccines (DoriVac) were fabricated with infectious-disease-specific peptides. a, Schematic of DoriVac, consisting of a DNA origami SQB nanoparticle conjugated with CpG at precise spacing of 3.5 nm and with infectious disease-specific peptides. **b**, Schematic demonstrating conjugation of DBCO-modified-oligonucleotide to an azide-modified peptide via copper-free click chemistry. **c**, (i) A schematic showing how HR2 protein mediates virus–host fusion; HR2 can serve as a conserved target for infectious-disease vaccines. (ii) Schematic showing how production of anti-HR2 antibodies (mAbs) prevents virus–host cell membrane fusion and thereby inhibits viral infection. **d**, Schematic of DNA origami SQB nanoparticles delivering antigen and adjuvant at a precise spacing to antigen presenting cells, eliciting both humoral and cellular immune responses. **e**, dPAGE gel showing successful conjugation and purification of infectious-disease-specific HR2 peptides to anti-handle oligonucleotides ('Oligo'). **f**, Agarose gel showing successful conjugation of oligo-HR2 peptides to the SQB DNA origami nanoparticles after removing the unconjugated cargos through PEG purification. **g**,**h**, SDS–PAGE gel showing the results after DNase I digestion of infectious disease-specific HR2 peptides alone (Pep) or conjugated with SQBs. DNase I digestion of the SQBs, followed by the analysis of the conjugated peptides using silver staining, confirms the successful peptide conjugation on the SQBs. DNase I sometimes produced a fainter secondary band with higher mobility. Additional gels with only DNase I and HIV-HR2 peptide are shown in Supplementary Fig. 1. **i**–**l**, Proposed schematics of the SQBs conjugated with CpGs (SQB-CpG) (**i**) and SQBs conjugated with CpGs (18 copies) and HR2 peptides (24 copies); CoV-2-HR2 DoriVac (**j**), HIV-HR2 DoriVac (**k**), Ebola-HR2 DoriVac (**l**)), respectively, and their representative TEM images. In TEM side views, the SQB exhibits two distinct faces: the flat interface is designated for CpG attachment, whereas the opposite face is reserved for peptide conjugation. The peptide-conjugated side is indicated by a red arrow in the first inset of each image set. The specific HR2 peptide sequences associated with each infectious disease are listed. Scale bars, 100 nm. Experiments in **e**–**l** were independently repeated two times with similar results. Illustrations created in BioRender: **b**,Young, O. https://BioRender.com/wex0e0z (2025); **c**(i), Young, O. https://BioRender.com/z94nwpj (2025); **c**(ii), Young, O. https://BioRender.com/emmmpvt (2025); **d**, Young, O. https://BioRender.com/9fyhh7q (2025).

https://doi.org/10.1038/s41551-026-01614-w

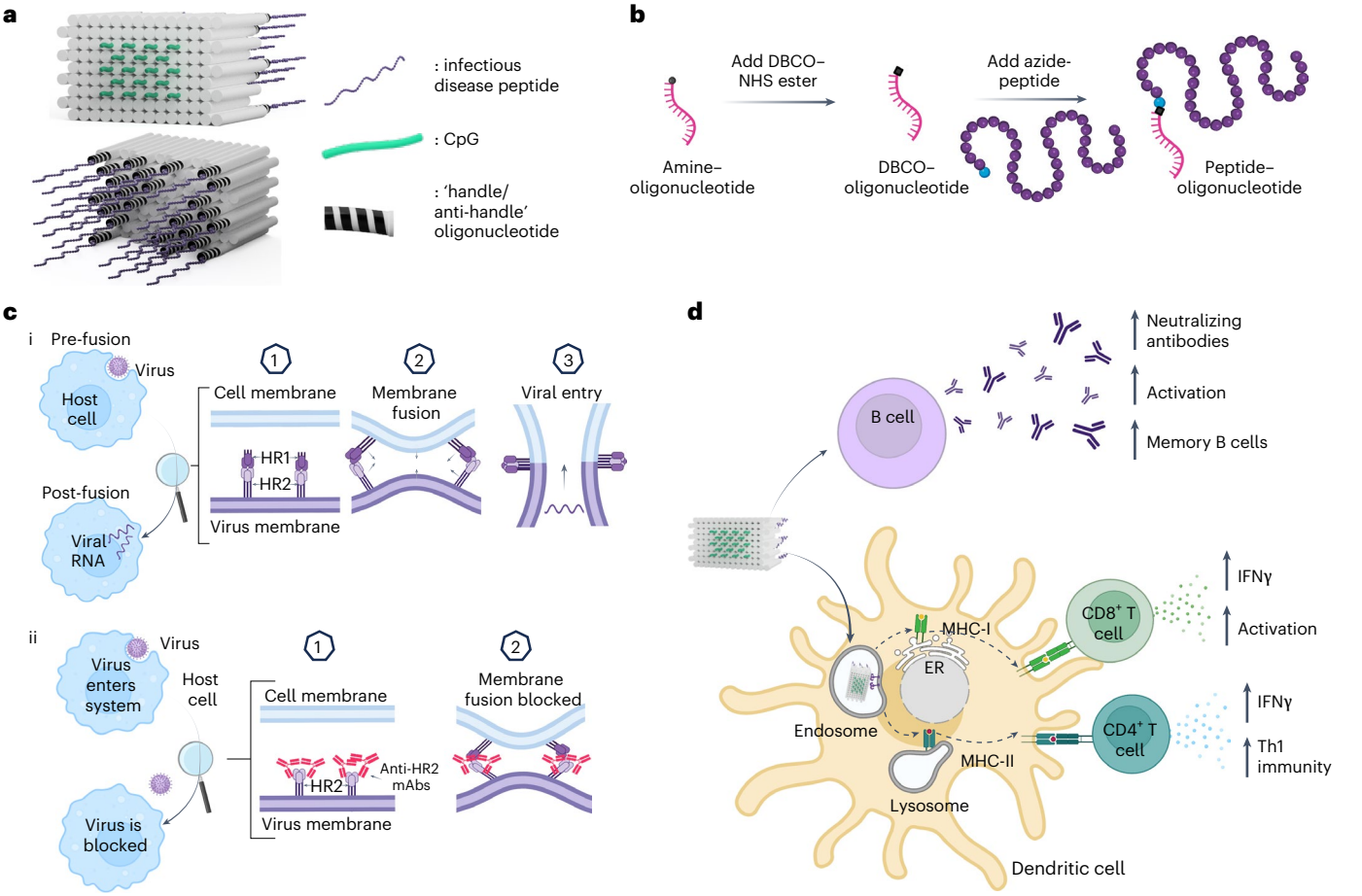

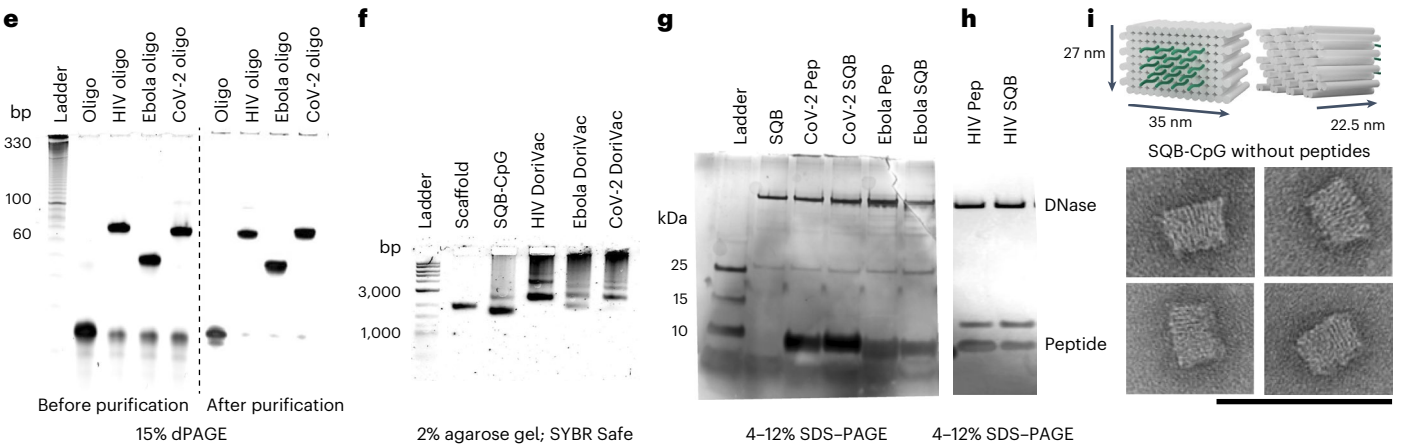

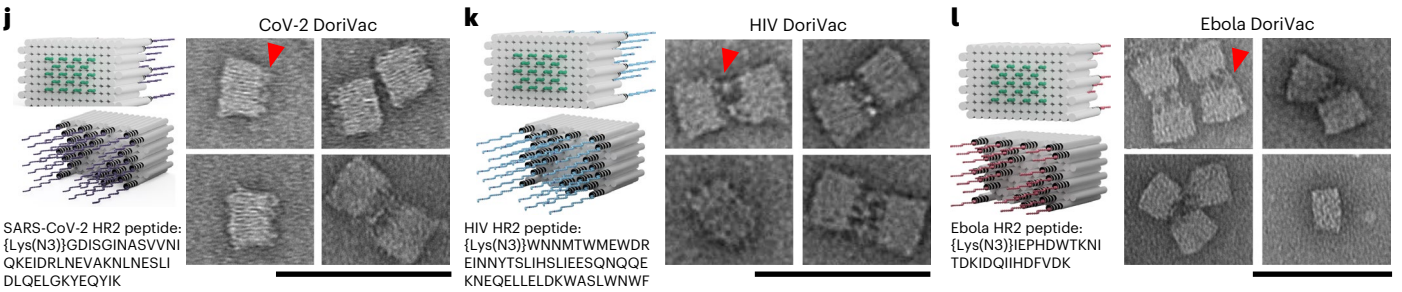

https://doi.org/10.1038/s41551-026-01614-w

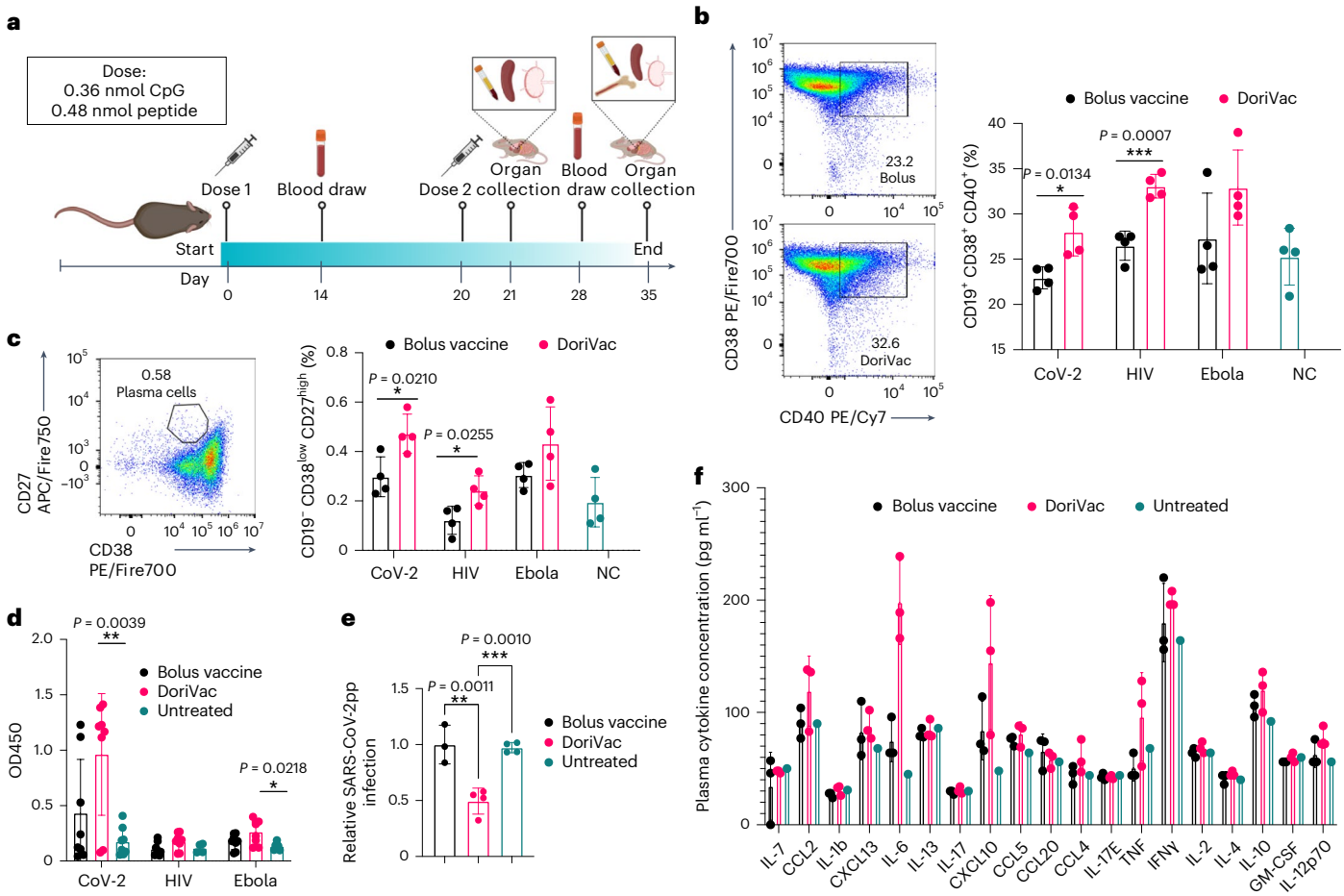

Fig. 2 | Immune profiling reveals the DoriVac elicits improved neutralizing antibody responses compared to a bolus vaccine. a, Schematic delineating the vaccine administration protocol for naive C57BL/6 mice and the data collection timeline. LNs and spleens were collected on day 21 and day 35 after killing the mice for flow cytometry and ELISpot analysis. Plasma was collected on days 14 and 28 for anti-HR2 antibody quantification and pseudovirus neutralization assays. Bone marrow and heart blood were collected at the conclusion of the study, day 35, to analyse B cell markers. **b**, B cells collected from the blood showed increased markers of activation and antigen-presentation capabilities (CD40) and memory capacity (CD38) after two doses of DoriVac treatment ($n = 4$) as determined by flow cytometry on day 21. NC, negative control. **c**, B cells collected from the blood on day 21 showed increased plasma-memory-cell population as evidenced by the increased $CD19^{-}$ $CD38^{low}$ $CD27^{high}$ subpopulation as determined by flow cytometry ($n = 4$). The number 0.58 refers to the gated frequency (%), i.e. the percentage of events within the parent (pre-gated) cell population that fall inside the polygon gate labelled 'Plasma cells'. **d**, DoriVac treatment enhanced HR2-specific IgG antibody production as evidenced by ELISA assay, after two doses of DoriVac (on day 35) compared to a bolus vaccine of free peptide and free CpG. Samples were diluted 1:100 before quantification. Data are normalized ($n = 8$). **e**, SARS-CoV-2pp neutralization assay (bolus vaccine $n = 3$; DoriVac and untreated $n = 4$, 1:100 dilution, day 28) in model cell line ACE2-293T. **f**, Plasma was collected 4 h after the first treatment dose on day 0. The inflammatory cytokine response was quantified via Luminex ELISA assay (Bio-Plex Pro Mouse Cytokine 20-plex Assay (Bio-Rad)) ($n = 3$ for treated groups; $n = 1$ for negative (that is, untreated) control). Data are represented as mean ± s.d. The pseudovirus and ELISA data were analysed by one-way ANOVA (with correction for multiple comparisons using a Tukey test), and significance was defined as a multiplicity-adjusted P value less than 0.05. The flow data were analysed by multiple unpaired t-tests, and significance was defined as a two-tailed P value less than 0.05. $^{*}P \leq 0.05$; $^{**}P \leq 0.01$; $^{***}P \leq 0.001$; bars without asterisks indicate no statistically significant difference except for **f** ($P > 0.05$). Unless otherwise indicated, n refers to samples from biologically independent mice. Illustration in **a** created in BioRender: Young, O. https://BioRender.com/nuox99v (2025).

especially in the case of the HIV and Ebola SQBs of which the majority are dimers, possibly due to hydrophobic peptide interactions.

DoriVac induces robust humoral immune responses

Having fabricated the vaccine, we evaluated DoriVac's efficacy for induction of both humoral and cellular immune responses in vivo. Naive mice were administered 20 pmol of HR2-fabricated DoriVac, comprising 0.36 nmol (2.2 μg) of CpG and 0.48 nmol of antigen (1.5–3.2 μg) (Fig. 2a). Two subcutaneous doses of DoriVac were given on day 0 and day 20, compared to bolus vaccine consisting of free CpG adjuvant and HR2 peptide. Blood samples were collected on days 14 and 28 for peripheral blood mononuclear cells (PBMCs) and plasma processing. On day 21, half of the mice from each group were killed for immune cell profiling (Supplementary Tables 4–6). On day 35, the remaining mice were killed for immune cell profiling.

On day 21, B cells from PBMCs exhibited increased CD40 expression, a marker of activation and antigen-presentation capacity, in all three DoriVac treatment groups (Fig. 2b), surpassing the bolus vaccine and suggesting that DoriVac is superior in inducing B cell activation. Day 35 revealed a heightened plasma memory B cell population in the bone marrow, as evidenced by an increased $CD19^{low}$ $CD38^{low}$ $CD27^{high}$ subpopulation after DoriVac treatment (Fig. 2c), despite unchanged overall B cell numbers (Supplementary Figs. 2 and 3). SARS-CoV-2-HR2 DoriVac treatment induced elevated HR2 peptide-specific IgG1 antibody responses, as quantified via enzyme-linked immunosorbent assay (ELISA), compared to the bolus vaccine (Fig. 2d

https://doi.org/10.1038/s41551-026-01614-w

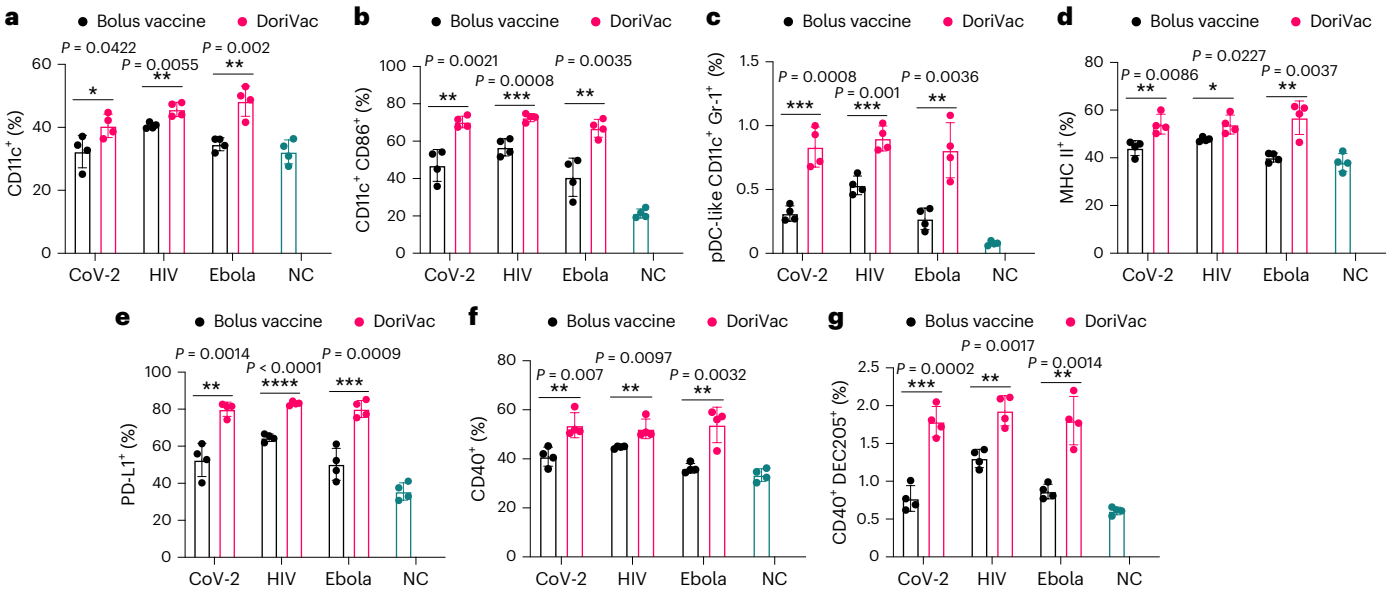

Fig. 3 | Immune profiling reveals DoriVac elicits superior antigen presenting cell responses compared to a bolus vaccine. C57BL/6 mice were treated with DoriVac (20 pmol) on day 0 and day 20. The mice were killed on day 21, and the draining LNs were processed into single-cell suspensions and analysed by flow cytometry. **a**, Percentages of $CD11c^+$ cells in the draining LNs ($n = 4$) were quantified. NC, negative control (that is, untreated). **b**, Percentages of $CD11c^+$ $CD86^+$ DCs in the draining LNs ($n = 4$) as determined by flow cytometry. **c**, Percentages of human pDC-like ($CD11c^+$ $Gr\text{-}1^+$) DCs in the draining LNs ($n = 4$) as determined by flow cytometry. **d**, Percentages of MHC-II^+ DCs in the draining LNs ($n = 4$) as determined by flow cytometry. **e**, Percentages of $PD\text{-}L1^+$ population in the draining LNs ($n = 4$) as determined by flow cytometry. **f**, Percentages of $CD40^+$ population in the draining LNs ($n = 4$) as determined by flow cytometry. **g**, Percentages of $CD40^+$ $DEC205^+$ population in DCs in the draining LNs ($n = 4$) as determined by flow cytometry. DoriVac showed a significant increase in DC activation compared to bolus-vaccine treatment. Data are represented as mean ± s.d. The flow data were analysed by multiple unpaired *t*-tests, and significance was defined as a two-tailed *P* value less than 0.05. $^*P \le 0.05$; $^{**}P \le 0.01$; $^{***}P \le 0.001$; $^{****}P \le 0.0001$.

and Supplementary Fig. 4). Neutralizing antibodies collected from SARS-CoV-2-HR2 DoriVac groups significantly reduced infection in a SARS-CoV-2 pseudovirus (SARS-CoV-2pp) assay (Fig. 2e). By contrast, we did not observe neutralization of the pseudovirus for HIV and Ebola in our assay, possibly due to the weak immunogenicity of the antigens associated with these viruses (Supplementary Tables 7–10). We did observe modest antigen-specific IgG1 responses for HIV and Ebola after HIV-HR-DoriVac and Ebola-HR2 DoriVac treatment, respectively (Fig. 2d and Supplementary Fig. 4). We examined initial cytokine responses 4 h after the first vaccine dose to naive mice (Fig. 2f). Type 1 cytokines (tumour necrosis factor (TNF), interleukin-2 (IL-2), interferon gamma (IFNγ), IL-12) were slightly elevated, while type 2 cytokines (IL-4, IL-10) exhibited no obvious elevation after DoriVac treatment compared to the bolus vaccine group and the untreated mice[59]. Overall, these findings affirm DoriVac's superior induction of humoral immune responses compared to those induced by a bolus vaccine, demonstrating its effectiveness in reducing the infection rate of SARS-CoV-2pp.

DoriVac induces DC activation

To ensure enduring immune protection against viral variants, a vaccine should stimulate both humoral and cellular immune responses. We first checked the DCs, which serve as a link between innate and adaptive immune responses. On day 21—1 day after the second vaccine dose—half of the mice were killed, and the draining lymph nodes (LNs) near the injection site were collected for flow (Supplementary Fig. 5). DoriVac increased the overall DC population (Fig. 3a) and activated DCs ($CD11c^+$ $CD86^+$) compared to the bolus vaccine (Fig. 3b). Plasmacytoid DCs (pDCs) are crucial in the anti-viral response in humans, secreting abundant type-1 interferon, fostering T cell activation and recruiting other immune cells[60]. The human pDC-like population ($CD11c^+$ $Gr\text{-}1^+$) significantly increased after DoriVac treatment (Fig. 3c), suggesting an increased anti-viral response. Activation markers MHC-II, programmed death-ligand 1 (PD-L1) and CD40 also increased after DoriVac administration (Fig. 3d–f). A notable rise was observed in the $CD40^+$ $DEC205^+$ DC population, indicating an increase in the activated, endocytic DC population (Fig. 3g). These results showed DoriVac induced robust activation of DCs in healthy mice (Supplementary Fig. 6). Furthermore, co-delivery of SQB and HR2 peptide did not elicit the same level of DC activation as observed with the delivery of HR2 peptide-conjugated SQBs (Supplementary Fig. 7). This observation is consistent with the outcomes previously noted in DoriVac studies involving tumour-bearing mice[52], further supporting the notion of the enhanced efficacy of the conjugated delivery system in activating DCs.

DoriVac shows activation of $CD4^+$ T cells

In our previous study involving DoriVac in mouse cancer models[52], we showed that DC activation by DoriVac leads to broad T cell activation. We aimed to confirm T cell induction by DoriVac in the context of viral antigens. Antigen-specific T cell activation was assessed via IFNγ enzyme-linked immunospot (ELISpot) assay on splenocytes; our results showed a significant increase in antigen-specific T cells after SARS-CoV-2-HR2 DoriVac administration (Fig. 4a,b). By contrast, HIV-HR2 DoriVac administration led to only a modest increase, and Ebola-HR2 DoriVac showed no apparent effect (Fig. 4a,b and Supplementary Fig. 8). We attribute this to the limited immunogenicity of the HR2 peptides used for HIV and Ebola, validated by their weaker predicted binding to MHC-I and MHC-II in both mice and humans via NetMHCpan-4.1 (ref. 61). By contrast, the SARS-CoV-2 HR2 peptide exhibited stronger binding predictions with six epitopes classified as strong binders, compared to zero to two epitopes for HIV and Ebola (Supplementary Tables 7–10). These findings underscore the importance of antigen selection in achieving effective antigen-specific T cell activation. These results confirmed that SARS-CoV-2-HR2 DoriVac induces significantly more antigen-specific T cells compared to the bolus vaccine.

Beyond overall T cell responses, we confirmed the presence of activated Th1 $CD4^+$ T cells via flow cytometry (Supplementary Fig. 9 for

https://doi.org/10.1038/s41551-026-01614-w

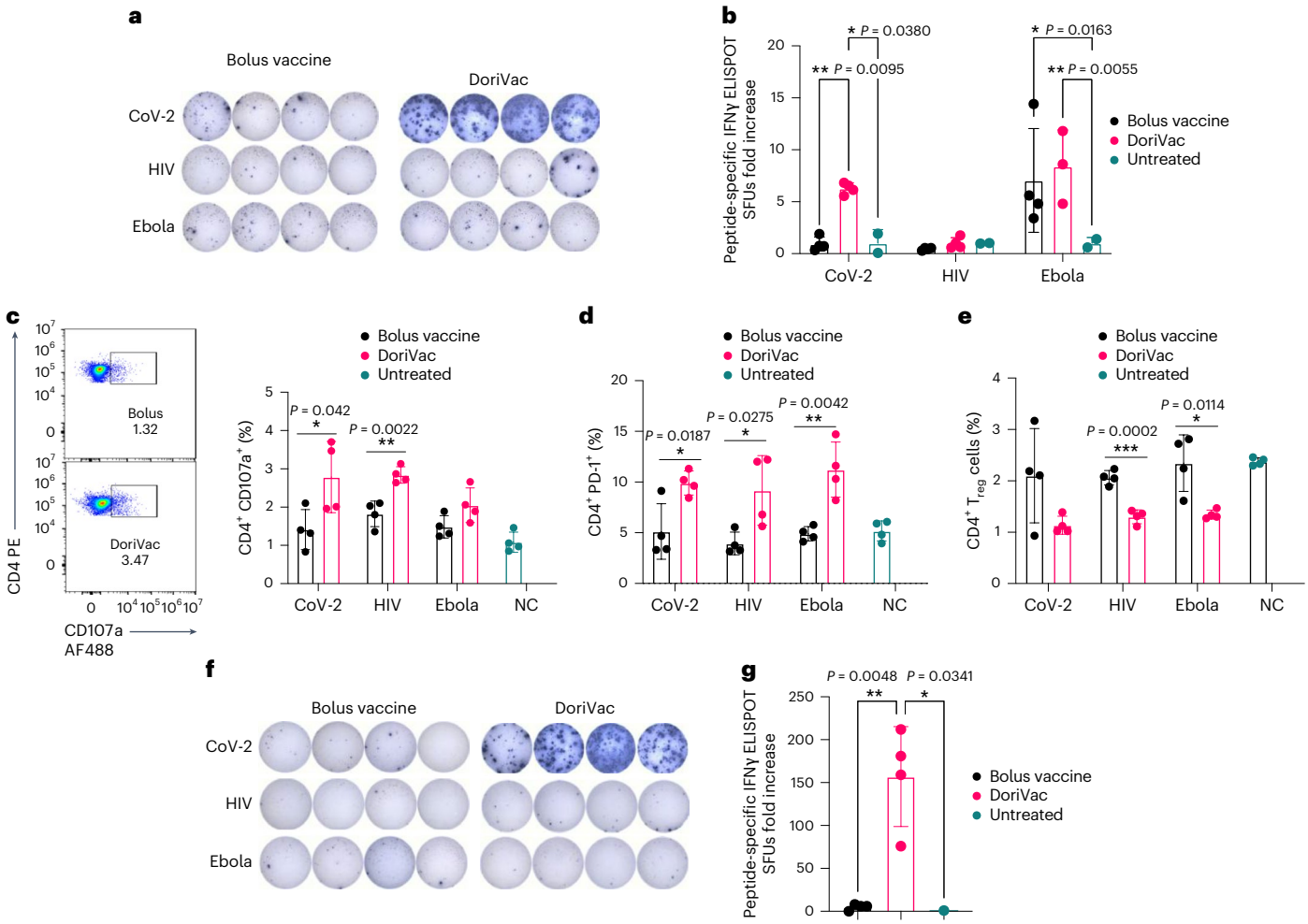

Fig. 4 | DoriVac induces enhanced Th1 CD4$^+$ T cell activation in mice. a, IFNγ ELISpot showing frequency of antigen-specific T cells in splenocytes on day 35 ($n = 4$) after treatment with DoriVac compared with the bolus vaccine. **b**, Quantification of IFNγ ELISpot spot forming units (SFUs, $n = 4$) shows significant increase in SARS-COV-2 antigen-specific T cell frequency after treatment with DoriVac compared with the bolus vaccine and negative control (that is, untreated). **c**, Percentages of CD4$^+$ CD107a$^+$ T cells in the LN ($n = 4$) as determined by flow cytometry and representative flow plots on day 35. **d**, Percentages of the LN CD4$^+$ PD-1$^+$ population ($n = 4$) as determined by flow cytometry on day 21. **e**, Percentages of LN CD4$^+$ T_{reg} population ($n = 4$) as determined by flow cytometry on day 21. **f**, IFNγ ELISpot showing frequency of CD4$^+$ enriched antigen-specific splenocytes ($n = 4$, day 35) after treatment with SARS-CoV-2-HR2 DoriVac. **g**, Corresponding quantification of IFNγ ELISpot SFUs ($n = 4$). Data are represented as mean ± s.d. The ELIspot data in **b** were analysed by two-way ANOVA (with correction for multiple comparisons using Tukey's test). The ELISpot data in **g** were analysed by one-way ANOVA (with correction for multiple comparisons using Tukey's test). In both analyses, statistical significance was defined as a multiplicity-adjusted P value less than 0.05. The flow data were analysed by multiple unpaired t-tests, and significance was defined as a two-tailed P value less than 0.05. *$P \leq 0.05$; **$P \leq 0.01$; bars without asterisks indicate no statistically significant difference ($P > 0.05$). Unless otherwise indicated, n refers to biologically independent mice.

gating strategy). CD107a notably increased in the CD4$^+$ T cell population, indicating enhanced CD4$^+$ T cell activation and increased cytotoxic potential (Fig. 4c)[62]. Programmed cell death protein 1 (PD-1) was also upregulated in the CD4$^+$ T cell population, showing increased activation (Fig. 4d). The regulatory T (T_{reg}) cell population significantly decreased after treatment with DoriVac, suggesting reduced immunosuppression (Fig. 4e). Antigen-specific CD4$^+$ T cell activation (CD8$^+$ T cells depleted by positive sorting) was quantified via IFNγ ELISpot, revealing a significant increase in antigen-specific activation after SARS-CoV-2 vaccination (Fig. 4f,g). These results verified activation of CD4$^+$ T cells, showing an antigen-specific immune response critical for immune memory.

DoriVac induces an antigen-specific CD8$^+$ T cell activation

Furthermore, after two vaccine doses, we confirmed activation of cytotoxic CD8$^+$ T cells. DoriVac increased the population of IFNγ-secreting cytotoxic CD8$^+$ T cells (Fig. 5a) and degranulating CD107a$^+$ CD8$^+$ T cells (Fig. 5b) in the LNs. PD-1 and CD69 were upregulated in the CD8$^+$ T cell population (Fig. 5c,d), indicating increased activation. On day 35, after the second dose, we quantified antigen-specific CD8$^+$ enriched T cells (CD4$^+$ T cell depleted by positive sorting) in the spleen via IFNγ ELISpot, showing increased antigen-specific CD8$^+$ T cells after SARS-CoV-2 DoriVac (Fig. 5e,f). Co-delivery of SQB, free HIV-HR2 peptide and free CpG did not induce a similar level of T cell activation as observed with the delivery of DoriVac (Supplementary Fig. 10).

Human immune-cell validation of peptide-conjugated and protein-conjugated DoriVac

Beyond murine models, we assessed DoriVac immunogenicity using a human LN organ-on-a-chip model. This model mimics the human LN for rapid prediction of vaccine responses in humans[63]. Analysing the impact of SARS-CoV-2-HR2 DoriVac on human monocyte-derived DCs, we observed increased CD86, CD40, human leukocyte antigen-DR (HLA-DR) and CD83 expression, indicating DoriVac can activate human DCs (Fig. 6a, Supplementary Table 11 and Supplementary Fig. 11).

https://doi.org/10.1038/s41551-026-01614-w

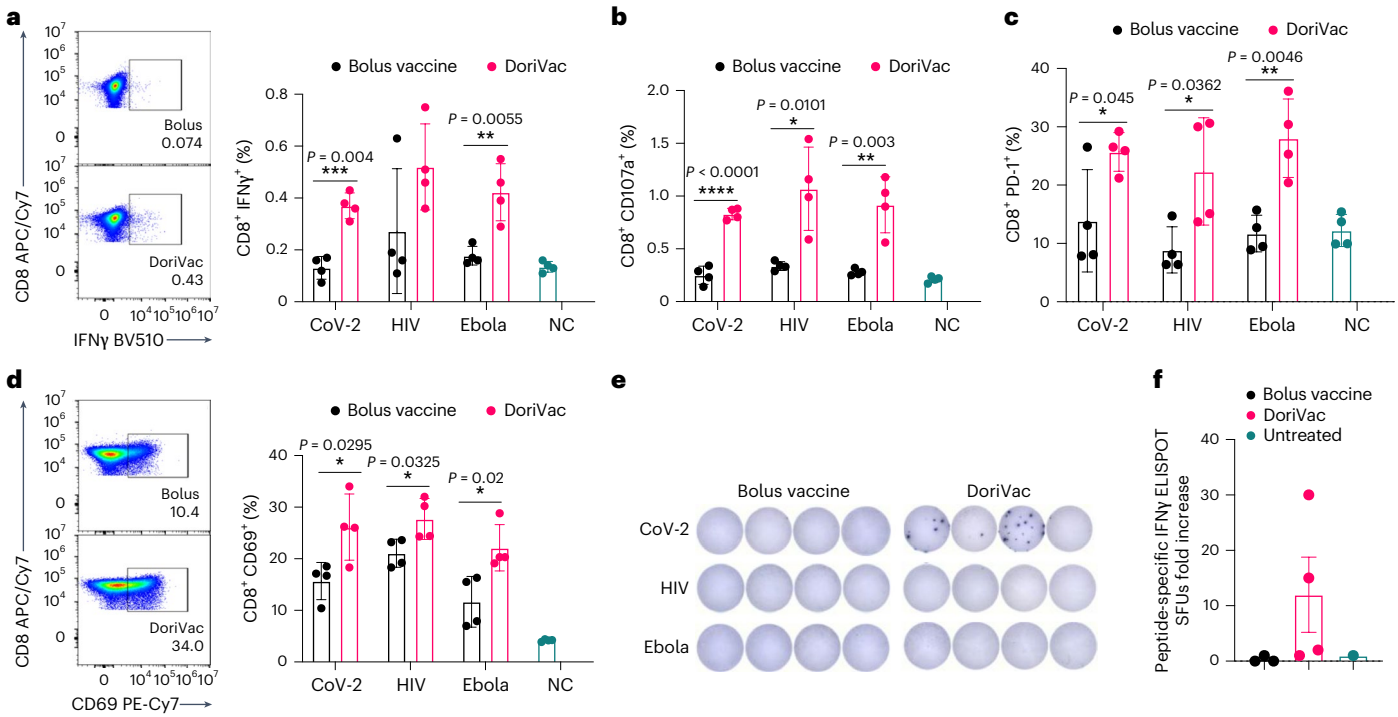

Fig. 5 | DoriVac induces enhanced antigen-specific CD8⁺ T cell activation in mice compared to bolus vaccine. a, Percentages of CD8⁺ IFNγ⁺ T cells in the LN ($n = 4$) on day 21 as determined by flow cytometry and representative flow plots from the SARS-CoV-2 data. **b**, Percentages of CD8⁺ CD107a⁺ T cells in the LN ($n = 4$) on day 21 as determined by flow cytometry. **c**, Percentages of CD8⁺ PD-1⁺ T cells in the LN ($n = 4$) on day 21 as determined by flow cytometry. **d**, Percentages of CD8⁺ CD69⁺ T cells in the LN ($n = 4$) on day 21 as determined by flow cytometry and representative flow plots. **e**,**f**, IFNγ ELISpot showing frequency of CD8⁺ enriched antigen-specific splenocytes ($n = 4$, day 35) (**e**), and accompanying quantification of IFNγ ELISpot SFUs (**f**) show a statistically significant increase in SARS-COV-2 antigen-specific CD8⁺ T cell frequency after treatment with DoriVac compared with the bolus vaccine. Data are represented as mean ± s.d. The flow data were analysed by multiple unpaired *t*-tests, and significance was defined as a two-tailed *P* value less than 0.05. The ELISpot data were analysed by one-way ANOVA (with correction for multiple comparisons using Tukey's test). Statistical significance was defined as a multiplicity-adjusted *P* value less than 0.05. $^{*}P \le 0.05$; $^{**}P \le 0.01$; $^{***}P \le 0.001$; $^{****}P \le 0.0001$; bars without asterisks indicate no statistically significant difference in tested conditions ($P > 0.05$). Unless otherwise indicated, *n* refers to biologically independent mice.

DoriVac treatment also elevated inflammatory cytokines secreted by DCs compared to the bolus (Fig. 6b). Analysing effector T cell responses on the human LN organ-on-a-chip model 9 days after vaccination, DoriVac showed a substantial increase in CD4⁺ and CD8⁺ T cell activation in two of the three donors, as evidenced by TNF⁺ and IL-2⁺ staining (Fig. 6c, Supplementary Table 12 and Supplementary Fig. 12). Polyfunctionality analysis (examining T cells that express IFNγ, TNF and IL-2) revealed more CD4⁺ polyfunctional cells induced by DoriVac than the bolus vaccine and an overall increase in CD8⁺ polyfunctional cells (Fig. 6d). Inflammatory cytokine analysis indicated similar levels induced by bolus and DoriVac across three donors (Fig. 6e). Furthermore, using a Meso Scale Discovery (MSD) assay to measure antibody production on the human LN organ-on-a-chip, we observed robust and broad antibody responses against SARS-CoV-2 spike variants in samples treated with HR2 peptide-conjugated DoriVac (Fig. 6f and Supplementary Fig. 13). These findings suggest that DoriVac induces a robust immune response in an in vitro human immune system that closely predicts human vaccine response.

We further expanded our investigation to showcase the versatility of DoriVac, enabling the conjugation of full-length viral protein antigens. Protein vaccines historically faced limitations in presenting antigens on MHC-I and inducing CD8⁺ T cell responses[64]. As a proof of concept, we selected hepatitis B surface antigen (HBsAg) and three monkeypox antigens (E8L, H3L and M1R), validated for prior immunogenicity in their respective diseases (Supplementary Table 13)[65,66].

The protein–anti-handle–oligonucleotide conjugate was synthesized using DBCO-azide click chemistry, where azide-modified oligonucleotide was conjugated to a protein via a DBCO-*N*-hydroxysuccinimidyl (NHS) ester linker (Fig. 6g). Successful conjugation was confirmed by sodium dodecyl sulfate (SDS)–PAGE gel (Fig. 6h,i). The protein–anti-handle–oligonucleotide conjugate was hybridized to the corresponding handle strands on the SQB via Watson–Crick base-pairing. Protein-conjugated DoriVac exhibited reduced mobility in agarose gel electrophoresis compared to unconjugated DNA origami (Fig. 6j). Successful protein conjugation was observed via SDS–PAGE gel analysis after DNase I digestion (relative to a protein-only control) (Fig. 6k,l).

Initially, we assessed T cell responses to HbsAg-conjugated DoriVac and bolus vaccine in the human LN organ-on-a-chip system 9 days after vaccination. DoriVac-stimulated DCs, pulsed with HBsAg, induced IFNγ secretion in both CD4⁺ and CD8⁺ subsets, showing antigen-specific T cell activation (Fig. 6m,n, Supplementary Table 12 and Supplementary Fig. 12). Polyfunctionality of T cells, measured by CD8⁺ T cells secreting IFNγ, TNF and IL-2, was higher for DoriVac than the bolus (Fig. 6o). To confirm successful T cell responses to DoriVac, we evaluated the immunogenicity of monkeypox antigens in a tonsil organoid model[67] from an independent donor, observing increased CD4⁺ IL-2⁺ and TNF⁺ effector T cells, as well as a higher percentage of IL-2⁺, TNF⁺ and IFNγ⁺ CD8⁺ T cells (Fig. 6p). These findings illustrate the capability of DoriVac to induce cellular immunity in humans against protein antigens of various infectious diseases.

DoriVac and mRNA–LNP vaccines elicited comparable immune responses in mice

To assess the DoriVac vaccine platform's suitability as protein antigen carrier and compare to commercially available mRNA–LNP vaccines, we fabricated DoriVac conjugated with complete SARS-CoV-2 spike

proteins and evaluated its immunogenicity alongside two bivalent mRNA–LNP vaccines (Fig. 7a,b and Supplementary Fig. 14). Specifically, we compared two physiologically relevant doses of DoriVac (20 pmol and 100 pmol; Supplementary Methods) to the bivalent vaccines (original and Omicron BA.4/BA.5) of mRNA-1273.222 (refs. 1,68) and BNT162b2-Omi.BA.4/BA.5 (refs. 3,69) (0.1 µg and 1 µg), hereafter mRNA-1273 and BNT162b2, in C57BL/6 mice (Fig. 7c). After the first booster dose on day 21, DoriVac at 100 pmol prompted greater DC mobilization in PBMCs than the mRNA vaccines for both tested doses (Fig. 7d and Supplementary Fig. 15), suggesting an early, potent induction of key antigen-presenting cells. On day 50 (1 day after the second booster), similar DoriVac-induced enhancements in DC activation and $CD11b^+$ cell mobilization were evident in the LNs and comparable to those of mRNA–LNP treatment groups (Supplementary Fig. 16), reflecting sustained antigen-presenting cell responses. All three vaccines elicited $CD4^+$ and $CD8^+$ effector and IFNγ-secreting T cells at similar levels in both PBMC (Supplementary Fig. 17) and lymphatic cell (Fig. 7e,f and Supplementary Fig. 18) populations. In addition, DoriVac-treated groups showed elevated CD69 expression on T cells in the LNs on day 50, at levels comparable to the mRNA–LNP treatment groups we tested (Supplementary Fig. 18). This observation suggested sustained activation within these primary immune sites, reinforcing that DoriVac's immune stimulation persisted after each booster. We also noted heightened NK cell activation and increased IFNγ expression for DoriVac treatment groups at both dosage levels on day 50, underscoring the breadth of DoriVac's immune engagement across multiple effector cell types (Supplementary Fig. 19). In addition, DoriVac-treated splenocytes and PBMCs produced high IFNγ levels comparable to those of mRNA–LNP vaccines at different time points upon ex vivo restimulation with SARS-CoV-2 peptides (Fig. 7g and Supplementary Fig. 20), underscoring a robust, antigen-specific T cell response across multiple tissue compartments. The specificity of these antibody responses were further validated against SARS-CoV-2 S1 domains (Supplementary Fig. 21) and spike proteins via ultra-sensitive single-molecule array (SiMoA)[70] (Fig. 7h and Supplementary Fig. 21) and pseudovirus neutralization assays (Fig. 7i and Supplementary Fig. 22). DoriVac elicited earlier and, at times, stronger antibody responses than the mRNA–LNP groups by day 22, highlighting a potentially faster humoral response under these dosing conditions. While showing comparable or higher immune activation, DoriVac did not induce the marked PD-1 upregulation observed in mice treated with 1 µg BNT162b2 (Supplementary Fig. 23), suggesting that DoriVac may induce reduced T cell exhaustion compared to BNT162b2 under our tested conditions. Finally, we assessed intramuscular administration and found similarly robust T cell responses with DoriVac, indicating route flexibility (Supplementary Fig. 24). Comparable to mRNA–LNP vaccines, DoriVac drove strong PBMC IFNγ responses up to 18 weeks after booster, emphasizing the sustained immunity generated by DoriVac (Supplementary Fig. 24). The day 91 (10 weeks post-booster) and day 147 (18 weeks post-booster) quantification of IFNγ-secreting cells from intramuscular administration showed intergroup comparisons comparable to the results from subcutaneous administration (Fig. 7g,j and Supplementary Figs. 20 and 24), underscoring DoriVac's robust and reproducible response over time. Despite fewer boosters and lower doses (10 pmol and 50 pmol, respectively), DoriVac consistently maintained IFNγ responses across extended time points, reinforcing its durable immunogenic profile. Consistent with reports of waning immunity in mRNA vaccines[71–75], the BNT162b2 1 µg vaccine treatment group saw a marked reduction in $IFN\gamma^+$ PBMC between day 91 and day 147, whereas the DoriVac treatment groups maintained fairly stable responses through the same interval. Moreover, to evaluate potential autoimmune or off-target responses, we measured anti-double-stranded-DNA and anti-polyethylene glycol (PEG) immunoglobulin G (IgG) 2 weeks and 10 weeks after the booster (day 35 and day 91), observing no significant increases compared to controls and thereby confirming DoriVac's favourable safety profile (Supplementary Fig. 25). Collectively, these findings reinforce DoriVac's promise as an effective DNA–protein vaccine platform capable of matching—and in certain measures surpassing—mRNA–LNP responses under our tested doses.

Fig. 6 | Peptide or protein-conjugated DoriVac effectively stimulates human DCs and induces enhanced immunogenicity compared to bolus vaccine on LN organ-on-a-chip model. a, Human monocyte-derived DCs were stimulated for 24 h with bolus or DoriVac, and the DC activation markers were analysed using flow cytometry. **b**, Relative fold changes in cytokines and chemokines after 24 h of human monocyte-derived DCs with bolus or DoriVac. Fold change relative to no treatment is shown. **c**, Graph quantifying polyfunctional T cells ($n = 3$), as determined by their ability to co-secrete IFNγ, TNF and IL-2 as determined via intracellular cytokine staining and flow cytometry. **d**, LN organ-on-a-chip ($n = 3$) were vaccinated with bolus or the SARS-CoV-2-HR2 DoriVac. Nine days after vaccination, T cell responses were assessed via intracellular cytokine staining and flow cytometry after ex vivo stimulation with SARS-CoV-2 HR2 peptide and phorbol 12-myristate 13-acetate (PMA)/ionomycin. Graphs quantifying the average cytokine-producing $CD4^+$ and $CD8^+$ T cell populations at 9 days after vaccination in three different donors. Each symbol represents one donor. **e**, Relative fold changes in IL-6, IL-8, IP-10, MIP-1β and TNF at 9 days after transduction either of the bolus or DoriVac on the LN organ-on-a-chip. Fold change relative to no treatment is shown. **f**, In a human LN organ-on-a-chip MSD assay, HR2 peptide-conjugated DoriVac induced a robust and broad antibody response against SARS-CoV-2 spike variants ($n = 3$) compared to untreated control. Observed (Obs.) concentrations were interpolated from the standard curve using a four-parameter logistic (4PL) regression. Other tested variants are shown in Supplementary Fig. 13. **g**, Schematic representation of protein–oligonucleotide conjugation, showing the utilization of DBCO–NHS ester crosslinker to attach an azide-modified oligonucleotide to the protein via free amine groups on lysines. **h**, SDS–PAGE gel (Coomassie-stained) confirming successful conjugation of monkeypox-specific proteins to oligonucleotides. Multiple bands in H3L-oligo and E8L conjugates indicate variable degrees of modification; M1R shifts slightly relative to the unconjugated protein. **i**, SDS–PAGE gel showing the successful conjugation of HBsAg proteins to oligonucleotides. **j**, Agarose gel verifying attachment of these oligo–protein complexes to the SQB DNA origami via handle–anti-handle hybridization. Conjugated SQB bands migrate more slowly than unconjugated SQB controls. **k**,**l**, Confirmation via SDS–PAGE gel of successful protein conjugation after DNase degradation of the DNA origami scaffold and staple strands and analysis of the remaining protein via silver stain: H3L and E8L (**k**); M1R (**l**). Each conjugation experiment in **h**–**l** was independently repeated thrice with consistent results confirmed by gel analysis. **m**–**o**, LN chips ($n = 2$) were vaccinated with bolus or DoriVac harbouring CpG and full-length HBsAg. The T cell responses were assessed using intracellular cytokine staining and flow cytometry after ex vivo stimulation with autologous DCs pulsed with HBsAg (1:10 effector/target ratio), 9 days after vaccination. Graphs quantify $IFN\gamma^+$ $CD4^+$ populations (**m**), $IFN\gamma^+$ $CD8^+$ populations (**n**) and $CD8^+$ polyfunctionality ($IFN\gamma^+$, TNF^+, $IL\text{-}2^+$) (**o**) in two different donors. **p**, Tonsil organoids from one donor were vaccinated with bolus or DoriVac harbouring CpG and full-length monkeypox antigens (E8L, H3L or M1R). T cell responses were assessed using intracellular cytokine staining and flow cytometry after ex vivo stimulation with 15-mer monkeypox antigenic peptides (overlapping by 11-mer) and PMA/ionomycin stimulation during the last 4 h of incubation. Graph quantifies the cytokine-producing effector $CD4^+$ and $CD8^+$ populations, 9 days after vaccination ($n = 3$ cell samples obtained from one preparation, treated with DoriVac fabricated with three different monkeypox antigens). The flow data for **c** and **d** were analysed by unpaired *t*-tests (two-tailed $P < 0.05$) and for **p** by multiple unpaired *t*-tests ($P < 0.05$). In all cases, $^*P \le 0.05$; $^{**}P \le 0.01$; bars without asterisks indicate no statistically significant difference ($P > 0.05$). Data are represented as mean ± s.d. Unless otherwise noted, n = biologically independent organ-on-a-chip cultures, one chip per human donor (three donors for **a**–**e**; two donors for **m**–**o**). For **f**, n = technical replicates: three chips from a single donor. For **p**, $n = 3$ independent tonsil organoid samples from a single donor.

https://doi.org/10.1038/s41551-026-01614-w

Discussion

Enduring immune memory and protection against viral variants rely on cellular immune responses, particularly $CD8^+$ T cells that target less mutable viral proteins. SARS-CoV-2 vaccines with greater than 90% protection showed induction of Th1-skewed immunity[76–81], emphasizing the importance of Th1 $CD4^+$ and $CD8^+$ T cell responses. In recent decades, DNA origami has achieved crucial milestones, indicating its potential as a modular therapeutic nanoparticle. Its programmability makes it a versatile 'plug-and-play' vaccine nanotechnology, particularly relevant for emerging infectious diseases. In this proof-of-concept study, HR2-DoriVac, conjugated with infectious-disease-associated peptides and proteins, elicited robust neutralizing antibodies and antigen-specific $CD4^+$ and $CD8^+$ T cell activation in healthy mice, a notable contrast to some SARS-CoV-2 vaccines with limited T cell responses. DoriVac presents distinct advantages including precise nanoscale arrangement of antigen and adjuvant for their co-delivery on each nanoparticle; well-established, simple and scalable fabrication; modular, programmable design adaptable for various antigens via DNA hybridization; and stability at 4 °C, contrasting with mRNA vaccines needing −20 °C to −80 °C cold chain storage[48]. Although we have not conducted a detailed cost analysis, DNA origami nanoparticles can potentially be produced at scale using established industrial processes, which may reduce manufacturing complexity and associated costs. Moreover, we have observed that DoriVac formulations remain stable at 4 °C for at least several weeks[52], offering logistical advantages over more stringent cold-chain requirements. Future studies focusing on

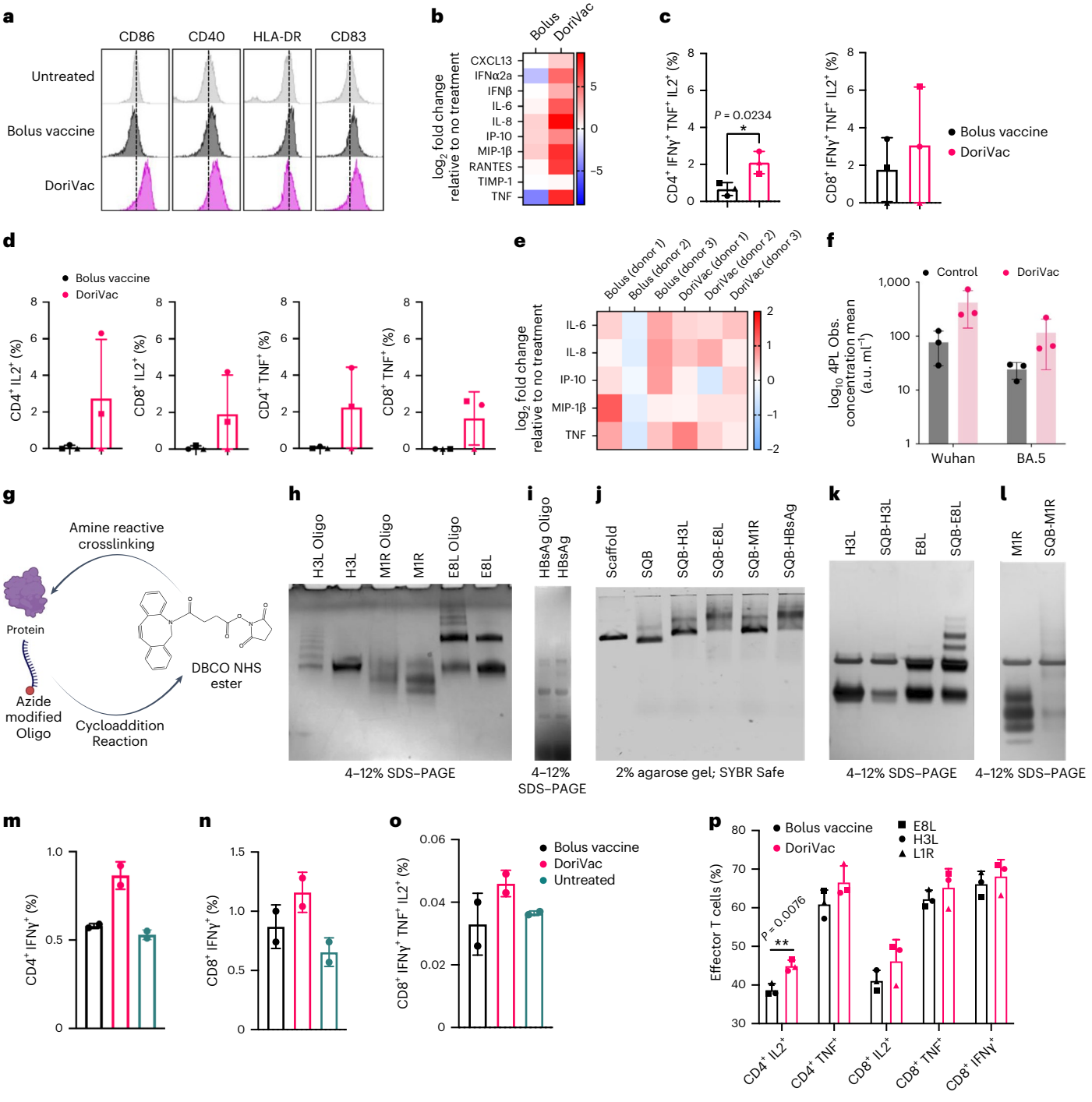

process optimization, long-term storage conditions and economies of scale will provide more quantitative data on cost-effectiveness and stability profiles, further informing DoriVac's potential as a practical and accessible vaccine platform.

While DNA origami allows us to precisely design cargo conjugation stoichiometry, the present study relied on DNase I digestion and PAGE-silver staining to validate conjugation efficiency; we acknowledge this approach provides only an approximation of cargo stoichiometry. In response, we have undertaken a separate investigation using gel-based and fluorescence-based techniques to more accurately quantify protein, peptide and nucleic acid cargo on DNA origami nanoparticles[82]. Integrating these improved methodologies, as well as mass spectrometry, into future DoriVac formulation analysis will facilitate standardized manufacturing protocols and ensure consistent vaccine quality.

While robust antigen-specific T cell activation was observed with SARS-CoV-2-HR2 DoriVac, the same level of activation was not achieved with HIV and Ebola DoriVac formulations. We observed that HIV-HR2 and Ebola-HR2 peptide-functionalized DoriVac nanoparticles tended to form dimers and aggregates, as evidenced by agarose gel electrophoresis and TEM imaging. This aggregation is likely attributed to the greater hydrophobicity of these particular HR2 sequences, which can promote intermolecular interactions between peptide-conjugated nanoparticles. However, whether such aggregation will reduce vaccine efficacy and accessibility to immune cells needs further investigation. In future implementations, an interior hollow cavity in the origami could be engineered for hosting of peptides[83], thereby mitigating aggregation. We have also explored the HIV and Ebola antigen epitopes prediction (Supplementary Tables 7–10), which showed fewer epitopes than CoV-2. While this may be the direct reason for the limited immune response, we acknowledge that binding affinity alone does not equate to actual peptide immunogenicity. Future in vitro and in vivo assays will be crucial to validate and refine these computational findings.

However, activation of B cells, DCs, $CD4^+$ and $CD8^+$ T cells for HIV and Ebola suggested a strong immune response, albeit possibly insufficient for protection from infection. The chosen antigens for HIV and Ebola are also predicted to be weakly immunogenic in humans (Supplementary Tables 14–17), so future studies could focus on identifying more immunogenic peptides for HIV and Ebola for presentation by human HLA alleles, potentially enhancing antigen-specific activation. Viral rechallenge studies, contingent on availability of biosafety level 3 (BSL-3) facilities, could further assess the effectiveness of DoriVac-induced immune activation against live viruses. In addition, while these results underscore DoriVac's architectural versatility, they also highlight that not all antigens yield comparable levels of immune activation. The platform's modular design ensures that the CpG-modified SQB scaffold and conjugation strategies can be easily adapted to different diseases; however, the ultimate efficacy depends on the intrinsic immunogenicity of the selected antigens. As a result, achieving consistently high efficiency across diverse pathogens may require antigen-specific optimizations and careful selection of epitopes to fully leverage DoriVac's modular potential.

Our head-to-head comparison of SARS-CoV-2 spike-conjugated DoriVac and mRNA–LNP vaccines underscores DoriVac's versatility and efficacy at the tested doses. By eliciting strong T cell and antibody responses with full-length spike protein, DoriVac shows adaptability in transitioning from peptide- to protein-based antigens, matching or potentially surpassing mRNA–LNP responses. Moreover, the complete spike protein encompasses a broader array of epitopes than short peptide fragments, which can further enhance overall immunogenicity by engaging multiple T and B cell clones. We observed a significant induction of PD-1 expression in the higher-dose BNT162b2-vaccinated group compared to those vaccinated with DoriVac, which may indicate a potential exhaustion of $CD8^+$ T cells in the higher-dose BNT162b2 group. Further mechanistic studies are warranted to clarify how this induction impacts long-term immune memory and informs vaccine design. These findings are dose dependent; however, only two doses were tested. A broader dose range and varied boosting intervals will be needed to identify optimal regimens and further assess DoriVac's relative performance. Systematic dose-ranging, multiple boosting schedules and evaluations against other protein-based vaccines will clarify where DoriVac excels and how it complements existing options. Comparisons under similar dosing with commercial protein-based vaccines could be used to evaluate DoriVac's real-world competitiveness and its benefits, including sustained immune responses and simpler storage. DoriVac's consistent performance via both subcutaneous and intramuscular routes highlights its flexibility, underscoring its potential to address mRNA–LNP limitations such as storage constraints.

Fig. 7 | SARS-CoV-2 spike-protein-conjugated DoriVac induces potent cellular and humoral immune activation in mice. a, SDS–PAGE gel verifying successful conjugation of SARS-CoV-2 spike proteins to oligonucleotides and the successful hybridization of spike-protein-conjugated oligonucleotides on the DoriVac SQB DNA origami. Experiment was independently repeated five times with similar results. **b**, Schematic representation of SARS-CoV-2 protein-conjugated DoriVac SQB and its negative-stained TEM images. Experiment was independently repeated five times with similar results. **c**, Schematic delineating the vaccine administration protocol for naive C57BL/6 mice and the data collection timeline. Blood samples were collected on day 1, day 22, day 35 and day 50. Plasma was separated for anti-SARS-CoV-2 antibody quantification and pseudovirus neutralization assays, while PBMCs were isolated for flow cytometry and ELISpot assay. Spleens and LNs were collected on day 35 and day 50, respectively, after killing the mice. **d**, Percentages of $CD103^+$, $CD86^+$, $Dec205^+$ and $CD103^+$ $Dec205^+$ double-positive $CD11c^+$ PBMCs ($n = 8$) on day 22 as determined by flow cytometry. Representative flow scatter plots are shown in Supplementary Fig. 15. DoriVac induced enhanced immune activation compared to controls, in some cases surpassing that of mRNA–LNPs. The flow data were analysed by one-way ANOVA. **e**,**f**, Percentages of $CD107a^+$ LN cells ($n = 4$) (**e**) and IFNγ-secreting cells ($n = 4$) (**f**) on day 50 as determined by flow cytometry. Representative flow scatter plots are shown in Supplementary Fig. 18. The DoriVac treatment group showed enhanced activation of these cells compared to the control and displayed comparative performance versus mRNA–LNP treatment groups. The flow data were analysed by one-way ANOVA. Data presented for **d**–**f** are mean ± s.e.m. **g**, IFNγ ELISpot showing frequency of antigen-specific splenocytes (left, $n = 4$, day 35), with accompanying quantification of IFNγ ELISpot spot forming units (SFUs) and mean spot sizes. The results show an increase in SARS-COV-2 antigen-specific T cell frequency after treatment with DoriVac compared to the control, with larger spots indicating robust cytokine release. **h**, Quantification of relative anti-spike IgG levels in plasma samples of control and DoriVac 100 pmol per mRNA–LNP 1 μg dose treatment groups using SiMoA ($n = 8$ on day 1 and day 22, $n = 4$ on day 35 and day 50). DoriVac treatment group exhibited increased antibody levels compared to the control across all sampling dates. On day 22, DoriVac also showed a significantly higher antibody level than mRNA–LNP treatment groups. Data for spike-specific DoriVac 100 pmol per mRNA–LNP 1 μg dose responses and S1-specific responses for both dosage levels can be viewed in Supplementary Fig. 21. **i**, SARS-CoV-2pp neutralization assay ($n = 8$ on day 1 and day 22, $n = 4$ on day 35 and day 50; 1:20 dilution) for DoriVac 20 pmol per mRNA–LNP 0.1 μg dose treatment groups in model cell line ACE2-293T. DoriVac showed stronger neutralizing capabilities from day 22 onward, compared to controls and, by day 50, to the tested mRNA–LNP groups. Additional data for other dilutions and dosages are available in Supplementary Fig. 22. **j**, Longitudinal IFNγ ELISpot showing SFUs of PBMCs following intramuscular administration reveals the lasting T cell responses in DoriVac-treated mice, extending to day 147, comparable to or exceeding those from mRNA–LNP groups (control $n = 4$, others $n = 2$). Data are represented as mean ± s.e.m., except in **h** as mean ± s.d. The data were analysed by one-way ANOVA (with correction for multiple comparisons using a Tukey's test), and significance was defined as a multiplicity-adjusted P value less than 0.05. NS, $P > 0.05$; $^{**}P \leq 0.01$; $^{***}P \leq 0.001$. Unless otherwise indicated, n refers to biologically independent mice. Illustration in **c** created in BioRender: Xiong, Q. https://BioRender.com/t43a180 (2025).

https://doi.org/10.1038/s41551-026-01614-w

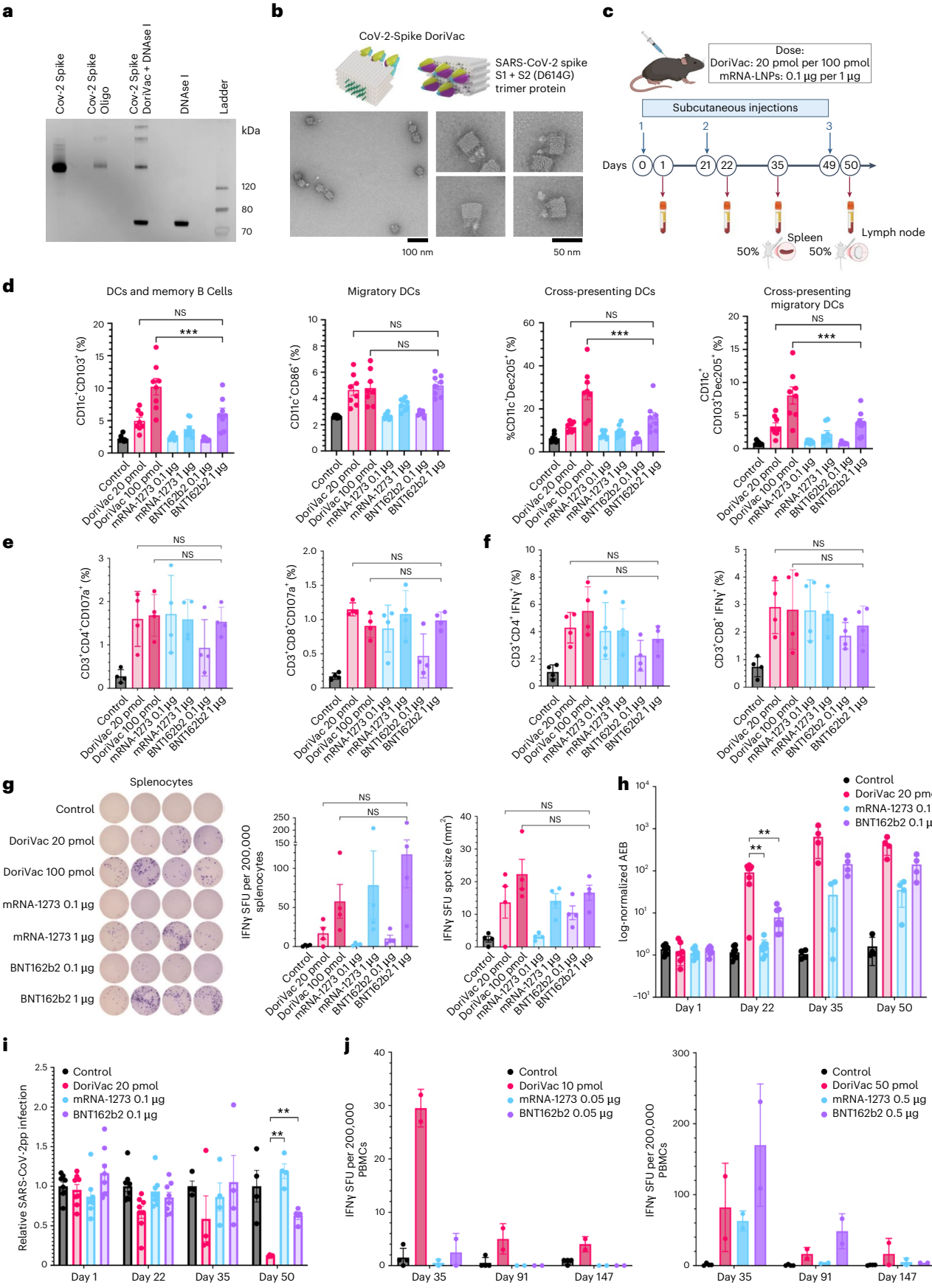

Future in vivo studies on long-term immunity and protective efficacy will further explore DoriVac's potential as an alternative, particularly given its capacity to incorporate other full-length proteins and adapt quickly to emerging pathogens.

This proof-of-concept study highlights DoriVac's capacity to rapidly generate vaccines against emerging infectious diseases and variants. Its programmable modularity supports multiplexed nanoparticles carrying diverse antigens, offering the promise of a versatile vaccine strategy. With a constant CpG-modified SQB scaffold, antigens can be readily exchanged, further supporting rapid adaptability across pathogens. This versatility positions DoriVac as a notable advancement for rapidly evolving infectious threats. Taken together, these attributes make DoriVac a promising next-generation platform that offers robust, sustained immune responses and simpler storage than current mRNA-based approaches.

Methods

SQB fabrication

SQB fabrication is detailed in a previous publication, including scaffold and staple sequences[52,84]. Scaffold p8634 was produced in-house, as previously published[85]. DNA staple strands were purchased from Integrated DNA Technologies (IDT). Folding concentrations were 5 mM Tris base, 1 mM ethylenediaminetetraacetic acid (EDTA; pH 8.0), 12 mM $MgCl_2$, 20–100 nM scaffold, 5 times excess of the basic staple strands (relative to scaffold concentration), 10 times excess of handle-conjugated staple strands (for attachment of relevant infectious-disease antigens) and 20 times excess CpG-staple strands. An 18 h thermocycler program was used to fabricate SQBs: denaturation at 80 °C for 15 min, then annealing via a temperature ramp from 50 °C to 40 °C decreasing at −0.1 °C every 10 min and 48 s. Most staple strands include ten thymidine residues at the end of the double helices to minimize aggregation. The CpG-containing strands were appended on the flat face of the SQB. The CpG oligonucleotides with nuclease-resistant phosphorothioate backbones (5′–TCCATGACGTTCCTGACGTT–3′, IDT) replaced the corresponding thymine residues in a 3.5 nm nanoscale pattern as determined previously[52]. CpG was appended to the 5′ ends of designated strands.

HR2 peptide conjugation with anti-handle oligonucleotide

An anti-handle oligonucleotide, which corresponds to 24 sites of handle oligonucleotide on the extruding face of the SQB, was ordered from IDT with a 5′ amine (aminoC6-TTCTAGGGTTAAAAGGGGACG). HR2 peptides were ordered from GenScript with an azide-modified N-terminal lysine (Fig. 1i–l and Supplementary Table 2) for DBCO-azide copper-free click chemistry reaction between the peptide and oligonucleotide. The oligonucleotide was prepared at 1 mM with phosphate buffer (pH 8.0). The DBCO–NHS ester (Millipore, 761524) (diluted in DMSO to 2 mM) was incubated with the oligonucleotide (diluted in phosphate buffer pH 8.0 to 100 µM) in 1:1 volume ratio and 1:20 oligonucleotides-to-DBCO ratio (with final concentration of DBCO > 1 mM) and incubated overnight at ambient temperature. The oligonucleotide–DBCO was purified via Illustra NAP column (GE Healthcare Life Sciences, 17-0852-02), eluted with sterile water and concentrated via 3K Amicon Ultra Centrifugal Filter Unit (Millipore, UFC500324). DBCO incorporation was confirmed via OD310 peak. Concentration was measured via A260 with the NanoDrop. The azide-modified HR2 peptides, representing SARS-CoV-2, HIV and Ebola, were dissolved in DMSO to 5 mM. The peptide-azide was mixed with the oligonucleotide–DBCO at a ratio of 1.5:1 and incubated overnight at room temperature in 1× PBS.

Denaturing PAGE verification and purification of peptide-conjugated oligonucleotide

To confirm peptide–oligonucleotide conjugation, 15% denaturing PAGE (dPAGE) was used. dPAGE gel (15%) was prepared using 9 ml urea concentrate (Fisher Scientific, EC-833), 4.5 ml urea dilutant, 1.5 ml urea buffer, 10 µl tetramethylethylenediamine and 150 µl 10 wt% ammonium persulfate in a casette (ThermoFisher Novex, NC2010)[52]. Then 5 pmol of the sample was mixed in a 1:1 ratio with formamide loading buffer and denatured at 80 °C for 10 min before loading into wells. Electrophoresis was carried out in 0.5× TBE buffer at 250 V for 45 min, followed by staining with SYBR Gold and imaging using the Typhoon Gel Scanner. For purification, the mixture was combined with formamide loading buffer, loaded into an 8% dPAGE gel in a large well formed using a taped comb, and run at 250 V for 50 min. The peptide–oligonucleotide was observed through UV shadowing on a thin-layer chromatography plate, excised, crushed and immersed in 1× TE buffer. After overnight shaking at 25 °C, purification was performed using Freeze 'N Squeeze DNA Gel Extraction Spin Columns (Bio-Rad, 7326165) and ethanol precipitation. The resulting peptide–oligonucleotide was resuspended in 1× PBS, and its concentration was determined using NanoDrop. Confirmation of purification was achieved via dPAGE.

Protein conjugation with anti-handle oligonucleotide

We generated protein–oligonucleotides by conjugating azide-modified DNA handles to the protein (obtained from Sino Biologic or Advanced ImmunoChemical; Supplementary Table 13) via the amino group present on lysine residues using DBCO-azide click chemistry. The reaction was incubated in phosphate buffer with a pH of 8.0 overnight at 4 °C and was subsequently agitated at 37 °C for 30 min. At higher pH levels (>8.0), NHS reactivity towards the ε-amino groups of lysines is enhanced compared to the α-amino group[86]. For gel quantification assays, the protein was simultaneously labelled with NHS-Cy3 dye. DTT was also added to the reaction to reduce any disulfide bonds.

For SARS-CoV-2 spike protein conjugations, the purified spike protein (Sino Biological, catalogue number 40589-V08H8, in phosphate buffer pH 8.0) was conjugated to azide-modified oligonucleotides similar to above but agitated longer at 37 °C for 60 min. Conjugation efficiency was assessed by SDS–PAGE and silver staining, and successful SQB attachment was confirmed via agarose gel electrophoresis and TEM.

Silver stain verification and purification of protein-conjugated oligonucleotide

Silver stain confirmed protein–oligonucleotide conjugation. The sample, mixed with 4× NuPAGE LDS sample buffer (ThermoFisher, NP0008), underwent incubation at 95 °C for 2 min before loading onto 4–12% NuPAGE Bis–Tris gels (ThermoFisher, NP0322) and electrophoresis at 150 V for 45 min in 1× MES SDS running buffer (ThermoFisher, NP0002). Gel analysis followed Pierce's (24612) silver staining protocol using Image Lab 6 on a Gel Doc EZ Imager (Bio-Rad). Purification used a 10K Amicon filter; the reaction sample, supplemented with phosphate buffer, was centrifuged at 14,000 × *g* for 30 min until the flow-through reached a DNA concentration of less than 1 ng μl^{-1}, indicating removal of all unconjugated DNA. Buffer exchange was carried out to 1× TE 10 mM $MgCl_2$.

Peptide- or protein-conjugated oligonucleotide hybridization with SQB

The peptide–oligonucleotides or protein–oligonucleotides were hybridized to the SQB DNA origami in a 2× excess, maintaining 10 mM $MgCl_2$ and 1× TE by adding stock 10× TE and 100 mM $MgCl_2$. SQBs were added last to ensure a consistent buffer environment. The resulting conjugated SQBs were incubated at 37 °C for 1–2 h with shaking, followed by purification through PEG precipitation. Analysis was performed using agarose gel electrophoresis, TEM and a DNase I degradation assay.

Agarose gel electrophoresis

SQBs were analysed via 2% native agarose gel electrophoresis. Gel was prepared with 0.5× TBE buffer with 11 mM $MgCl_2$ and 0.005% *v*/*v*

SYBR Safe (ThermoFisher, S33102), run at 70 V for 2 h, and imaged via a Typhoon Gel Scanner.

TEM analysis

TEM was used to assess structural integrity and SQB aggregation using negative-stain techniques. Formvar-coated, carbon-stabilized grids, either self-prepared or obtained from Electron Microscopy Services (FCF200-CU-TA), were plasma-discharged for 30 s for passivation. Subsequently, 4–10 nM SQBs were deposited on the grids for 45 s, followed by blotting with filter paper. Uranyl-formate solution (0.75% *w*/*v* in H_2O) was applied to the grid and blotted off, and a second application lasted for 2 min before blotting. Imaging of the grids occurred using a JEOL JEM-1400 TEM in brightfield mode at 120 kV.

SQB purification via PEG precipitation

CpG-SQBs or peptide- or protein-conjugated CpG-SQBs were purified via PEG precipitation. Then 1× TE buffer (5 mM Tris base, pH 8.0 and 1 mM EDTA acid) containing 15% *w*/*v* PEG-8000 (Fisher Scientific, BP2331) and 510 mM NaCl was added to the SQB sample at 1:1 volume and mixed gently via pipetting. $MgCl_2$ stock was added to the PEG solution to achieve 10 mM $MgCl_2$ final concentration. As described previously, the solution was incubated for 30 min then centrifuged at 16,000 × *g* for 25 min, and the supernatant was removed[52]. This procedure purifies and concentrates the sample, as a high concentration is often required for further studies. The concentration was determined via Nanodrop; the sample purity and integrity were confirmed via agarose gel electrophoresis and TEM.

DNase I degradation and silver stain analysis of conjugation efficiency

For analysis of conjugation efficiency, 1 µg of SQBs was incubated with 1.0 U μl^{-1} DNase I (NEB) with 10× DNase I buffer diluted in water (New England Biolabs, M0303S). Samples were incubated in the thermocycler for 30 min at 37 °C. Silver staining was performed as described above. ImageJ (v1.54g) was used to quantify band intensities and determine peptide or protein loading efficiencies.

K10-PEG5k coating of SQBs

Before administration, PEG-purified peptide- or protein-conjugated SQBs were mixed with oligolysine-PEG5k (K10-PEG5k; methoxy-poly(ethylene glycol)-block-poly(L-lysine hydrochloride); $n = 113, x = 10$; Alamanda Polymers (mPEG20K-b-PLKC10)) based on the calculated number of phosphates in the SQB sequence. An appropriate quantity of K10-PEG5k was added to match the number of nitrogens in its amines with the SQB phosphates, following a previously published method[87]. The mixture underwent incubation at 37 °C for at least 30 min, and concentration was determined based on dilution.

Animal model and treatment

C57BL/6 mice (6–8 weeks old) were obtained from Jackson Laboratory and housed at the Harvard Medical School animal facility. Eight groups of eight mice each underwent the following treatments: (1) SARS-CoV-2-HR2 DoriVac, (2) SARS-CoV-2 HR2 bolus, (3) HIV-HR2 DoriVac, (4) HIV-HR2 bolus, (5) Ebola-HR2 DoriVac, (6) Ebola-HR2 bolus, (7) SQB-CpG + free HIV-HR2 peptide and (8) untreated. The bolus contained an equivalent dose of CpG and HR2 peptide in PBS. Following 1 week acclimation, mice received the first treatment dose (100 µl of DoriVac containing 0.36 nmol of CpG and 0.48 nmol of HR2 peptide) subcutaneously on days 0 and 20. Blood was drawn via submandibular vein puncture 4 h after dosing and also on days 14, 20 and 28. On days 21 and 35, four mice from each group were killed; heart blood, LNs, spleens and femurs were collected. All procedures were approved by the Harvard Medical School Institutional Animal Care and Use Committee. mRNA–LNP vaccines (mRNA-1273.222 and BNT162b2-Omi.BA.4/BA.5) were diluted in sterile DPBS to the indicated doses before administration. Subcutaneous or intramuscular (right hind leg; quadriceps femoris) injections were performed using fresh preparations to maintain vaccine integrity.

Lymph-node-on-a-chip and tonsil organoid vaccination

For the fabrication of the lymph-node-on-a-chip, primary human lymphocytes were isolated from peripheral blood by density gradient centrifugation. T cells, B cells and monocytes were purified using StemCell isolation kits and combined at a ratio of 49:49:2. These cells were resuspended at a density of 2 million cells per 15 µl of 3D hydrogel and seeded into a microfluidic Emulate Chip S-1, which allows continuous superfusion with complete RPMI-based medium to recreate the three-dimensional and fluidic microenvironment of lymphoid tissue. Cells were cultured under flow conditions, during which they reaggregated and self-assembled into lymphoid follicle-like structures. Physiological perfusion was maintained using the Emulate Zoe-CM1 module[63]. Cryopreserved human tonsil single-cell suspensions were washed, counted and resuspended at high density in complete RPMI-based medium. For organoid formation, 2 million cells were plated onto permeable membrane supports in 24-well Transwell inserts and cultured at 37 °C with 5% CO_2 (ref. 67). Both lymph-node-on-a-chip and tonsil organoid cultures were treated with 1 nM of vaccine. Human patient-derived apheresis collars and tonsils were obtained from the Crimson Biomaterials Collection Core Facility under Harvard University Institutional Review Board approval, with all samples de-identified and donors providing informed consent in accordance with ethical guidelines. In LN chip experiments, RPMI medium supplemented with 10% FBS, 1% antibiotics, IL-2 and IL-4 was circulated for 14 days. Medium was recirculated every 2–3 days. Four and 9 days after the start of perfusion, 50% of the perfusion medium was replaced with fresh medium containing IL-2 and IL-4. Culture outflows at day 14 were collected to assess antibody responses against SARS-CoV-2 spike variants. Tonsil organoid cultures received fresh medium in a 1:1 ratio on day 4. At study conclusion, cells were collected by blocking one basal channel port and manually pipetting Cell Recovery Medium (Corning, 354253; 200 µl per chip) through the other to extract extracellular matrix and cells, which were then depolymerized, centrifuged and resuspended for further analysis.

Processing blood cells

Blood was collected either via heart extraction or through a submandibular cheek draw into heparin-coated tubes. Plasma and blood cells were separated via centrifugation at 800 × *g* and 4 °C for 5 min. The collected plasma was stored at −80 °C until analysis, while the blood cells underwent treatment with red blood cell lysis buffer (10×) from BioLegend (420301) three times, following the manufacturer's protocol. PBMCs were subsequently analysed using ELISpot and/or flow cytometry (Cytoflex LX).

Luminex multiplex ELISA analysis

The customized Bio-Plex Pro Mouse Cytokine Standard 23-plex kit from Bio-Rad included the following cytokines: IL-1α, IL-1β, IL-2, IL-3, IL-4, IL-5, IL-6, IL-9, IL-10, IL-12p40, IL-12p70, IL-13, IL-17A, Eotaxin, G-CSF, GM-CSF, IFNγ, MCP-1, MIP-1α, MIP-1β, RANTES, TNF, following the manufacturer's protocol. Data collection was performed using the Bio-Plex 3D Suspension Array System (Bio-Rad).

Processing LNs

Following euthanasia, the upper axillary and superficial cervical LNs from the mouse were collected and stored in cold PBS, as previously outlined[52]. These LNs were processed into single-cell suspensions for flow cytometry analysis (Cytoflex LX) by gently mashing them through a 40 µm cell strainer using a sterile syringe plunger into a petri dish. Cells were collected into 1.5 ml Eppendorf tubes, centrifuged at 400 g for 5 min at 4 °C, and the supernatant was discarded. The cell pellet was resuspended in 700 µl of PBS and distributed into 96-well plates for flow cytometry analysis.

Processing spleens

Following euthanasia, mouse spleens were collected, washed with PBS, and mashed through a 40 µm cell strainer into a 60 mm petri dish using a sterile syringe plunger. The resulting single-cell suspension was washed with complete RPMI-1640 media (containing 10% fetal bovine serum and 1% penicillin-streptomycin), collected into a Falcon tube, and subjected to two treatments with red blood cell lysis buffer (BioLegend, 420301) following the manufacturer's protocol. The cell pellet was resuspended in 2 ml of complete RPMI media, and the cell count was determined. These splenocytes were used for flow cytometry or ELISpot assays.

Processing bone marrow

Following euthanasia, femurs were repeatedly washed with PBS. Muscle fibres and connective tissues were extracted using forceps. Marrow extraction involved flushing the bone with a syringe into a PBS-filled dish. The collected marrow clot was pipetted, filtered through a 40 µm cell strainer, and gathered into a Falcon tube. The resulting single-cell suspension underwent centrifugation at 300 × *g* for 5 min. After discarding the supernatant, the pellet was treated with red blood cell lysis buffer (BioLegend, 420301) following the manufacturer's instructions. The suspension was centrifuged at 300 × *g* for 5 min and subsequently resuspended in culture media for flow cytometry (Cytoflex LX).

Flow cytometry

Single-cell suspensions of LNs, PBMCs, spleens and bone marrow were obtained. The suspensions were washed with PBS, stained with Zombie UV (BioLegend, 423108) or ViaKrome 808 (Beckman Coulter, C36628) viability dye and washed with cell staining buffer (BioLegend, 420201). The cells were stained with fluorophore-conjugated cell surface antibodies (Supplementary Tables 4–6, 11, 12 and 18). Intracellular staining was performed using permeabilization and fixation reagents (BioLegend, 424401). Antibodies were arranged into appropriate panels, compensations were set up to minimize fluorescent emission overlap, and the cells were analysed on a Cytoflex LX flow cytometer. Storage events were gated on the population of interest, based on protocols published previously[52], and according to the gating in Supplementary Figs. 2, 5, 9, 11, 12, 16, 18 and 19. Flow data were analysed using FlowJo V10.

CD8 and CD4 enrichment of splenocytes

Splenocytes were depleted for $CD4^+$ or $CD8^+$ T cells using CD8 Dynabeads (Thermofisher, 11145D) or CD4 Microbeads (Miltenyi Biotec, 130-117-043), according to manufacturer's instructions. The remaining sample was enriched for $CD4^+$ T cells (via $CD8^+$ T cell depletion) or enriched for $CD8^+$ T cells (via $CD4^+$ T cell depletion). Splenocytes were maintained in 4 °C for 36 h before processing for $CD8^+$ T cell enrichment. For CD8 depletion, the Dynabeads were washed in isolation buffer and placed in the magnet. At the same time, cells were prepared at a concentration of 1×10^7 cells per ml in isolation buffer. The prewashed beads were added, and the solution was incubated for 30 min at 4 °C with gentle tilting. Afterwards, the tubes were placed in the magnet for 2 min, and the supernatant was transferred to a new tube for further analysis. The beads and associated cells were discarded. Regarding CD4 depletion via microbeads, the cells were incubated with the microbeads for 10 min at 4 °C and then processed through an LD column (Miltenyi Biotec), yielding the CD8-enriched (CD4-depleted) population in the flow-through for subsequent analysis.

IFNγ ELISpot

Samples were processed into single-cell suspensions, followed by plating PBMCs or splenocytes into a 96-well round-bottom plate, each containing cells from an individual mouse in 200 µl of media. The cell quantities used were the following: two and a half million cells for splenocytes on day 21, three million cells for splenocytes on day 35, two million cells for PBMCs, eight and a half million cells for CD4 and CD8 enriched samples and two hundred thousand cells for full-length SARS-CoV-2 Spike DoriVac and mRNA–LNP assays. Each well was stimulated with 2 µg ml^{-1} of HR2 peptide or 1.67 µg ml^{-1} SARS-CoV-2 peptide pools (Miltenyl Biotec, 130-127-951, 130-132-051). For HR2 peptide experiments, after 48 h of incubation, cells were collected, resuspended in 100 µl of sterile media and plated onto an ELISpot plate (RND systems, Mouse IFNγ ELISpot kit, 505841) to incubate for 36 h at 37 °C. Cells from full-length SARS-CoV-2 Spike DoriVac and mRNA–LNP animal experiments were directly plated with stimulating peptides on an ELISpot plate and incubated for 20 h at 37 °C. The plate was then processed as per the manufacturer's guidelines and analysed using an ELISpot plate reader at Dana Farber Cancer Institute's Center for Immuno-oncology Translational Immunogenics Laboratory.

ELISA

Plasma IgG from vaccinated mice was quantified using an ELISA method. Nunc Maxisorp ELISA plates (ThermoFisher, 44-2404-21) were coated with HR2 peptide at a concentration of 2–20 µg ml^{-1} in 100 µl of coating buffer (100 mM bicarbonate/carbonate buffer, pH 9.5) and incubated overnight at 4 °C. After washing three times with washing buffer (PBS containing 0.05% Tween 20), 150 µl of blocking buffer (2% bovine serum albumin (Sigma, 9048-46-8) in washing buffer) was applied for 1 h at 37 °C. After removing the blocking buffer, 100 µl of plasma samples diluted in blocking buffer (1:100, 1:200, 1:400 dilutions) was added and incubated for 1 h at 37 °C. After washing three times with washing buffer, 150 µl of blocking buffer was applied for 1 h at 37 °C. After removing the blocking buffer, 100 µl of HRP-conjugated anti-mouse IgG antibody (Cell Signaling Technology, 7076) diluted in blocking buffer was applied for 1 h at 37 °C. After washing five times with washing buffer, 50 µl of 3,3′,5,5′-tetramethyl benzidine substrate (Sigma, 54827-17-7) for detection was added, and the reaction was stopped after 15 min by the addition of 50 µl of 1 M H_2SO_4. Absorbance at 450 nm was measured using an automated plate reader (BioTek).

Pseudovirus assay

Plasma was isolated by collecting the clear supernatant after centrifugation. Samples were diluted in culture media at varying ratios and cultured with the corresponding pseudovirus and ACE2-293 T cells. Relative pseudovirus infection level was assessed as the ratio of infected cells in each group to those in the bolus or the control group, which was assigned a relative infection level of 1.0.

SiMoA

Multiplexed SiMoA assays were used to measure anti-SARS-CoV-2 IgG antibodies against the S1 subunit of the spike protein, the full spike protein and nucleocapsid protein (control), as previously described[70]. The collected mouse serum samples were diluted 4,000-fold and analysed using an automated three-step assay format onboard an HD-X analyser (Quanterix). In the first step, the diluted serum samples are incubated with SARS-CoV-2 antigen-conjugated fluorescent beads. Then the beads are washed and incubated in a solution of 1 ng ml^{-1} biotinylated anti-mouse IgG antibody (Abcam, ab6788) in the second step. The beads are washed again and incubated in a solution of 30 pM of streptavidin-β-galactosidase in the third step. Afterwards, the beads are resuspended in a solution of resorufin β-D-galactopyranoside and loaded into a microwell array for analysis. Average enzyme per bead (AEB) values were calculated by the HD-X analyser and normalized between runs using a control solution of a neutralizing anti-spike mouse monoclonal antibody (Sino Biological, 40591-MM43) at a concentration of 5 pg ml^{-1}.

Assay for anti-dsDNA and anti-PEG IgG

Anti-dsDNA and anti-PEG IgG levels were measured using the Mouse Anti-dsDNA IgG ELISA Kit (catalogue number 5120, Alpha Diagnostic International) and the Mouse Anti-PEG IgG ELISA Kit (catalogue number

PEG-030, Alpha Diagnostic International), respectively. Both assays were performed according to the manufacturers' protocols. Briefly, all kit-provided calibrators, samples and positive controls were assayed in duplicate. Serum samples were diluted 1:100 in the supplied sample diluent, consistent with the recommended dilution of ≥1:100. After appropriate incubations and washes, the bound IgGs were detected with an anti-mouse IgG–HRP conjugate followed by TMB substrate development and measurement of optical density at 450 nm with normalization at 630 nm. Data analysis was carried out according to the manufacturers' guidelines for each kit.

SARS-CoV-2 spike-specific immunoglobulin quantitation in LN chip outflows

Anti-SARS-CoV-2 IgG concentrations were determined in day 14 LN chip outflows via the 10-PLEX MSD V-PLEX SARS-CoV-2 Spike Panel 27 (IgG) Kit (K15606U). Assays were performed according to the manufacturer's specifications. Briefly, LN chip outflows were tested in duplicate at 1:10, 1:70 and 1:490 dilutions, with samples incubated on plates pre-coated with spike antigens from multiple SARS-CoV-2 variants ($n = 10$); antibody binding was detected with SULFO-Tag-labelled anti-human IgG antibody. Data were acquired with an MSD Meso Sector S 600MM plate reader and analysed with MSD Discovery Workbench 4.0 software. Sample antibody concentrations (arbitrary units per millilitre (a.u. ml^{-1})) were calculated against the kit-provided standard (using four-parameter logistic regression), reporting data from the dilution nearest to the midpoint of the curve. Concentrations are reported for Wuhan and BA.5 spike variants in Fig. 6f, with data from additional variants reported in Supplementary Fig. 13, including B.1.351 (beta variant), B.1.617.2; AY.4 Alt Seq 2 (delta variant), BA.2, BA.2.12.1, BA.2 + L452M, BA.2 + L452R, BA.3 and BA.4 (Omicron sublineage variants). Three positive controls, containing known levels of SARS-CoV-2-specific IgG, were included in the kit and tested to confirm assay performance. CH65 IgG human monoclonal antibody[88], specific to influenza receptor binding site haemagglutinin glycoprotein, served as a negative control.

Statistical analyses

One-way or two-way analysis of variance (ANOVA) or unpaired *t*-test(s) with appropriate corrections for multiple comparisons as detailed in the figure captions was applied to determine the statistical significance of all flow, ELISpot and ELISA data in Figs. 2–7. GraphPad Prism 10 was used to make graphs, analyse statistics and calculate *P* values. $P \leq 0.05$ was considered statistically significant; $^{*}P \leq 0.05$; $^{**}P \leq 0.01$; $^{***}P \leq 0.001$; $^{****}P \leq 0.0001$. Error bars represent standard deviation (s.d.).

Reporting summary

Further information on research design is available in the Nature Portfolio Reporting Summary linked to this article.

Data availability

Data supporting the findings of this study are presented in the paper and the Supplementary Information. Source data are provided with this paper.

References

1. Baden, L. R. et al. Efficacy and safety of the mRNA-1273 SARS-CoV-2 vaccine. *N. Engl. J. Med.* **384**, 403–416 (2021).
2. Folegatti, P. M. et al. Safety and immunogenicity of the ChAdOx1 nCoV-19 vaccine against SARS-CoV-2: a preliminary report of a phase 1/2, single-blind, randomised controlled trial. *Lancet* **396**, 467–478 (2020).
3. Polack, F. P. et al. Safety and efficacy of the BNT162b2 mRNA Covid-19 vaccine. *N. Engl. J. Med.* **383**, 2603–2615 (2020).
4. Sadoff, J. et al. Safety and efficacy of single-dose Ad26.COV2.S vaccine against Covid-19. *N. Engl. J. Med.* **384**, 2187–2201 (2021).
5. Keech, C. et al. Phase 1-2 trial of a SARS-CoV-2 recombinant spike protein nanoparticle vaccine. *N. Engl. J. Med.* **383**, 2320–2332 (2020).
6. Tegally, H. et al. Detection of a SARS-CoV-2 variant of concern in South Africa. *Nature* **592**, 438–443 (2021).
7. Cherian, S. et al. SARS-CoV-2 spike mutations, L452R, T478K, E484Q and P681R, in the second wave of COVID-19 in Maharashtra, India. *Microorganisms* **9**, 1542 (2021).
8. Viana, R. et al. Rapid epidemic expansion of the SARS-CoV-2 Omicron variant in southern Africa. *Nature* **603**, 679–686 (2022).
9. Geers, D. et al. SARS-CoV-2 variants of concern partially escape humoral but not T-cell responses in COVID-19 convalescent donors and vaccinees. *Sci. Immunol.* **6**, eabj1750 (2021).
10. Garcia-Beltran, W. F. et al. Multiple SARS-CoV-2 variants escape neutralization by vaccine-induced humoral immunity. *Cell* **184**, 2523 (2021).
11. Hoffmann, M. et al. SARS-CoV-2 variant B.1.617 is resistant to bamlanivimab and evades antibodies induced by infection and vaccination. *Cell Rep.* **36**, 109415 (2021).
12. Madhi, S. A. et al. Efficacy of the ChAdOx1 nCoV-19 Covid-19 vaccine against the B.1.351 variant. *N. Engl. J. Med.* **384**, 1885–1898 (2021).
13. Wang, Z. et al. mRNA vaccine-elicited antibodies to SARS-CoV-2 and circulating variants. *Nature* **592**, 616–622 (2021).
14. Wibmer, C. K. et al. SARS-CoV-2 501Y.V2 escapes neutralization by South African COVID-19 donor plasma. *Nat. Med.* **27**, 622–625 (2021).
15. Wu, K. et al. Serum neutralizing activity elicited by mRNA-1273 vaccine. *N. Engl. J. Med.* **384**, 1468–1470 (2021).
16. Si, L. et al. Triterpenoids manipulate a broad range of virus-host fusion via wrapping the HR2 domain prevalent in viral envelopes. *Sci. Adv.* **4**, eaau8408 (2018).
17. Chambers, P., Pringle, C. R. & Easton, A. J. Heptad repeat sequences are located adjacent to hydrophobic regions in several types of virus fusion glycoproteins. *J. Gen. Virol.* **71**, 3075–3080 (1990).
18. Harrison, S. C. Viral membrane fusion. *Nat. Struct. Mol. Biol.* **15**, 690–698 (2008).
19. Chan, D. C., Fass, D., Berger, J. M. & Kim, P. S. Core structure of gp41 from the HIV envelope glycoprotein. *Cell* **89**, 263–273 (1997).
20. Joshi, S. B., Dutch, R. E. & Lamb, R. A. A core trimer of the paramyxovirus fusion protein: parallels to influenza virus hemagglutinin and HIV-1 gp41. *Virology* **248**, 20–34 (1998).
21. Malashkevich, V. N. et al. Core structure of the envelope glycoprotein GP2 from Ebola virus at 1.9-A resolution. *Proc. Natl Acad. Sci. USA* **96**, 2662–2667 (1999).
22. Ma, X. et al. Nanoparticle vaccines based on the receptor binding domain (RBD) and heptad repeat (HR) of SARS-CoV-2 elicit robust protective immune responses. *Immunity* **53**, 1315–1330.e1319 (2020).
23. Elshabrawy, H. A., Coughlin, M. M., Baker, S. C. & Prabhakar, B. S. Human monoclonal antibodies against highly conserved HR1 and HR2 domains of the SARS-CoV spike protein are more broadly neutralizing. *PLoS ONE* **7**, e50366 (2012).
24. Grifoni, A. et al. Targets of T cell responses to SARS-CoV-2 coronavirus in humans with COVID-19 disease and unexposed individuals. *Cell* **181**, 1489–1501.e1415 (2020).
25. He, C. et al. A self-assembled trimeric protein vaccine induces protective immunity against Omicron variant. *Nat. Commun.* **13**, 5459 (2022).
26. Kyriakidis, N. C., López-Cortés, A., González, E. V., Grimaldos, A. B. & Prado, E. O. SARS-CoV-2 vaccines strategies: a comprehensive review of phase 3 candidates. *NPJ Vaccines* **6**, 28 (2021).
27. Nelde, A. et al. SARS-CoV-2-derived peptides define heterologous and COVID-19-induced T cell recognition. *Nat. Immunol.* **22**, 74–85 (2021).

28. Rodda, L. B. et al. Functional SARS-CoV-2-specific immune memory persists after mild COVID-19. *Cell* **184**, 169–183.e117 (2021).
29. Tan, A. T. et al. Early induction of functional SARS-CoV-2-specific T cells associates with rapid viral clearance and mild disease in COVID-19 patients. *Cell Rep.* **34**, 108728 (2021).
30. Dan, J. M. et al. Immunological memory to SARS-CoV-2 assessed for up to 8?months after infection. *Science* **371**, eabf4063 (2021).
31. Le Bert, N. et al. SARS-CoV-2-specific T cell immunity in cases of COVID-19 and SARS, and uninfected controls. *Nature* **584**, 457–462 (2020).
32. Braun, J. et al. SARS-CoV-2-reactive T cells in healthy donors and patients with COVID-19. *Nature* **587**, 270–274 (2020).
33. Mateus, J. et al. Selective and cross-reactive SARS-CoV-2 T cell epitopes in unexposed humans. *Science* **370**, 89–94 (2020).
34. Riou, C. et al. Escape from recognition of SARS-CoV-2 variant spike epitopes but overall preservation of T cell immunity. *Sci. Transl. Med.* **14**, eabj6824 (2022).
35. Moss, P. The T cell immune response against SARS-CoV-2. *Nat. Immunol.* **23**, 186–193 (2022).
36. Zhao, J. et al. Airway memory CD4(+) T cells mediate protective immunity against emerging respiratory coronaviruses. *Immunity* **44**, 1379–1391 (2016).
37. Peng, Y. et al. Broad and strong memory CD4. *Nat. Immunol.* **21**, 1336–1345 (2020).
38. Sekine, T. et al. Robust T cell immunity in convalescent individuals with asymptomatic or mild COVID-19. *Cell* **183**, 158–168.e114 (2020).
39. McMahan, K. et al. Correlates of protection against SARS-CoV-2 in rhesus macaques. *Nature* **590**, 630–634 (2021).
40. Friedrich, T. C. et al. Subdominant CD8+ T-cell responses are involved in durable control of AIDS virus replication. *J. Virol.* **81**, 3465–3476 (2007).
41. Chowdhury, A. et al. Differential impact of in vivo CD8+ T lymphocyte depletion in controller versus progressor simian immunodeficiency virus-infected macaques. *J. Virol.* **89**, 8677–8686 (2015).
42. Sullivan, N. J. et al. CD8+ cellular immunity mediates rAd5 vaccine protection against Ebola virus infection of nonhuman primates. *Nat. Med.* **17**, 1128–1131 (2011).
43. Woldemeskel, B. A., Garliss, C. C. & Blankson, J. N. SARS-CoV-2 mRNA vaccines induce broad CD4+ T cell responses that recognize SARS-CoV-2 variants and HCoV-NL63. *J. Clin. Invest.* **131**, e149335 (2021).
44. Bai, J. et al. Early CD4. *Sci. Rep.* **12**, 20376 (2022).
45. Oberhardt, V. et al. Rapid and stable mobilization of CD8. *Nature* **597**, 268–273 (2021).
46. Kuse, N. et al. Long-term memory CD8. *Nat. Commun.* **13**, 5251 (2022).
47. Comberlato, A., Paloja, K. & Bastings, M. M. C. Nucleic acids presenting polymer nanomaterials as vaccine adjuvants. *J. Mater. Chem. B* **7**, 6321–6346 (2019).
48. Vu, M. N., Kelly, H. G., Kent, S. J. & Wheatley, A. K. Current and future nanoparticle vaccines for COVID-19. *EBioMedicine* **74**, 103699 (2021).
49. Pati, R., Shevtsov, M. & Sonawane, A. Nanoparticle vaccines against infectious diseases. *Front. Immunol.* **9**, 2224 (2018).
50. Igyártó, B. Z., Jacobsen, S. & Ndeupen, S. Future considerations for the mRNA-lipid nanoparticle vaccine platform. *Curr. Opin. Virol.* **48**, 65–72 (2021).
51. Du, R. R. et al. Innate immune stimulation using 3D wireframe DNA origami. *ACS Nano* **16**, 20340–20352 (2022).
52. Zeng, Y. C. et al. Fine tuning of CpG spatial distribution with DNA origami for improved cancer vaccination. *Nat. Nanotechnol.* **19**, 1055–1065 (2024).
53. Liu, S. et al. A DNA nanodevice-based vaccine for cancer immunotherapy. *Nat. Mater.* **20**, 421–430 (2021).
54. Sun, Y. et al. DNA origami–based artificial antigen-presenting cells for adoptive T cell therapy. *Sci. Adv.* **8**, eadd1106 (2022).
55. Oktay, E., Alem, F., Hernandez, K., Narayanan, A. & Veneziano, R. DNA origami presenting the receptor binding domain of SARS-CoV-2 elicit robust protective immune response. *Commun. Biol.* **6**, 308 (2023).
56. Veneziano, R. et al. Role of nanoscale antigen organization on B-cell activation probed using DNA origami. *Nat. Nanotechnol.* **15**, 716–723 (2020).
57. Zhang, J. et al. Elucidating the effect of nanoscale receptor-binding domain organization on SARS-CoV-2 infection and immunity activation with DNA origami. *J. Am. Chem. Soc.* **144**, 21295–21303 (2022).
58. Sun, Y. et al. Nanoscale organization of two-dimensional multimeric pMHC reagents with DNA origami for $CD8^+$ T cell detection. *Nat. Commun.* **13**, 3916 (2022).
59. Karupiah, G. Type 1 and type 2 cytokines in antiviral defense. *Vet. Immunol. Immunopathol.* **63**, 105–109 (1998).
60. Fitzgerald-Bocarsly, P., Dai, J. & Singh, S. Plasmacytoid dendritic cells and type I IFN: 50 years of convergent history. *Cytokine Growth Factor Rev.* **19**, 3–19 (2008).
61. Reynisson, B., Alvarez, B., Paul, S., Peters, B. & Nielsen, M. NetMHCpan-4.1 and NetMHCIIpan-4.0: improved predictions of MHC antigen presentation by concurrent motif deconvolution and integration of MS MHC eluted ligand data. *Nucleic Acids Res.* **48**, W449–W454 (2020).
62. Takeuchi, A. & Saito, T. CD4 CTL, a cytotoxic subset of CD4. *Front. Immunol.* **8**, 194 (2017).
63. Goyal, G. et al. Ectopic lymphoid follicle formation and human seasonal influenza vaccination responses recapitulated in an organ-on-a-chip. *Adv. Sci.* **9**, e2103241 (2022).
64. Rock, K. L. & Shen, L. Cross-presentation: underlying mechanisms and role in immune surveillance. *Immunol. Rev.* **207**, 166–183 (2005).
65. Cohn, H. et al. Mpox vaccine and infection-driven human immune signatures: an immunological analysis of an observational study. *Lancet Infect. Dis.* **23**, 1302–1312 (2023).
66. Cooper, C. & Mackie, D. Hepatitis B surface antigen-1018 ISS adjuvant-containing vaccine: a review of HEPLISAV™ safety and efficacy. *Expert Rev. Vaccines* **10**, 417–427 (2011).
67. Wagar, L. E. et al. Modeling human adaptive immune responses with tonsil organoids. *Nat. Med.* **27**, 125–135 (2021).
68. Chalkias, S. et al. A Bivalent Omicron-Containing Booster Vaccine against Covid-19. *N. Engl. J. Med.* **387**, 1279–1291 (2022).
69. Usdan, L. et al. A bivalent Omicron-BA.4/BA.5-adapted BNT162b2 booster in >/=12-year-olds. *Clin. Infect. Dis.* **78**, 1194–1203 (2024).
70. Norman, M. et al. Ultrasensitive high-resolution profiling of early seroconversion in patients with COVID-19. *Nat. Biomed. Eng.* **4**, 1180–1187 (2020).
71. Naaber, P. et al. Dynamics of antibody response to BNT162b2 vaccine after six months: a longitudinal prospective study. *Lancet Reg. Health Eur.* **10**, 100208 (2021).
72. Nanishi, E., Levy, O. & Ozonoff, A. Waning effectiveness of SARS-CoV-2 mRNA vaccines in older adults: a rapid review. *Hum. Vaccin. Immunother.* **18**, 2045857 (2022).
73. Lassauniere, R. et al. Neutralizing antibodies against the SARS-CoV-2 Omicron variant (BA.1) 1 to 18 weeks after the second and third doses of the BNT162b2 mRNA vaccine. *JAMA Netw Open* **5**, e2212073 (2022).
74. Brook, B. et al. Adjuvantation of a SARS-CoV-2 mRNA vaccine with controlled tissue-specific expression of an mRNA encoding IL-12p70. *Sci. Transl. Med.* **16**, eadm8451 (2024).
75. Nguyen, D. C. et al. SARS-CoV-2-specific plasma cells are not durably established in the bone marrow long-lived compartment after mRNA vaccination. *Nat. Med.* **31**, 235–244 (2025).
76. Luan, N. et al. Th2-oriented immune serum after SARS-CoV-2 vaccination does not enhance infection. *Front. Immunol.* **13**, 882856 (2022).

77. Corbett, K. S. et al. Evaluation of the mRNA-1273 vaccine against SARS-CoV-2 in nonhuman primates. *N. Engl. J. Med.* **383**, 1544–1555 (2020).
78. Laczkó, D. et al. A single immunization with nucleoside-modified mRNA vaccines elicits strong cellular and humoral immune responses against SARS-CoV-2 in mice. *Immunity* **53**, 724–732. e727 (2020).
79. Jackson, L. A. et al. An mRNA vaccine against SARS-CoV-2 - preliminary report. *N. Engl. J. Med.* **383**, 1920–1931 (2020).
80. Walsh, E. E. et al. Safety and immunogenicity of two RNA-based Covid-19 vaccine candidates. *N. Engl. J. Med.* **383**, 2439–2450 (2020).
81. Corbett, K. S. et al. SARS-CoV-2 mRNA vaccine design enabled by prototype pathogen preparedness. *Nature* **586**, 567–571 (2020).
82. Young, O. J., et al. Cargo quantification of functionalized DNA origami for therapeutic application. *Small Methods* **9**, e2401376 (2024).
83. Wickham, S. F. J. et al. Complex multicomponent patterns rendered on a 3D DNA-barrel pegboard. *Nat. Commun.* **11**, 5768 (2020).
84. Ke, Y. et al. Multilayer DNA origami packed on a square lattice. *J. Am. Chem. Soc.* **131**, 15903–15908 (2009).
85. Douglas, S. M., Chou, J. J. & Shih, W. M. DNA-nanotube-induced alignment of membrane proteins for NMR structure determination. *Proc. Natl Acad. Sci. USA* **104**, 6644–6648 (2007).
86. Nanda, J. S. & Lorsch, J. R. Labeling a protein with fluorophores using NHS ester derivitization. *Methods Enzymol.* **536**, 87–94 (2014).
87. Ponnuswamy, N. et al. Oligolysine-based coating protects DNA nanostructures from low-salt denaturation and nuclease degradation. *Nat. Commun.* **8**, 1–9 (2017).
88. Whittle, J. R. et al. Broadly neutralizing human antibody that recognizes the receptor-binding pocket of influenza virus hemagglutinin. *Proc. Natl Acad. Sci. USA* **108**, 14216–14221 (2011).

Acknowledgements

We appreciate the support and experimental input from Shih Lab members. Special thanks to K. Mulligan, M. Perez, M. Carr, T. Ferrante and E. Zigon for their expertise with instrumentation. We also thank J. B. Flechtner for her insights during results discussions and her assistance with figure preparation. Figure1b-d, Fig.2a, Fig.7c, and Supplementary Fig.24a were generated using BioRender (https://biorender.com/). We thank the Harvard University Health Services for sharing the unused portion of mRNA–LNP vaccines (mRNA-1273.222 and BNT162b2-Omi.BA.4/BA.5) from opened vials to enable the comparative studies of DoriVac and mRNA–LNP vaccines. W.M.S., Y.C.Z and O.J.Y disclose support for the research described in this study from the Claudia Adams Barr Program at Dana-Farber Cancer Institute and the Director's Fund and Validation Fund from Wyss Institute at Harvard University, in addition to support from a US National Institutes of Health (NIH) U54 grant (CA244726-01) and the US–Japan Civilian Research and Development Foundation (CRDF) Global Fund (R-202105-67765). J.H.R. and I.C.K. acknowledge support from the National Research Foundation of Korea grants funded by the Korean government (MSIT; RS-2024-00463774, RS-2023-00275456) and the Intramural Research Program of the Korea Institute of Science and Technology. M.W.K., G.G., and D.E.I. disclose support for the research using human organ-on-a-chip from the Bill and Melinda Gates Foundation (INV-002274) and Wyss Institute for Biologically Inspired Engineering at Harvard University. G.D.T. acknowledges support for research using human organ-on-a-chip from Gates Foundation (INV-060822). Q.X. acknowledges support from the Agency for Science, Technology and Research (A*STAR) Singapore through the A*STAR International Fellowship. H.D. acknowledges support from the Fujifilm Fellowship and the Herchel Smith Fellowship. S.H.S. acknowledges support from the Korea Health Technology R&D Project through the Korea Health Industry Development Institute, funded by the Ministry of Health & Welfare, Republic of Korea (RS-2023-00269815).

Author contributions

Y.C.Z. and L.S. developed the idea. Y.C.Z., O.J.Y., Q.X., L.S. and M.W.K. planned experiments. O.J.Y. and Q.X. fabricated and tested the vaccine. Y.C.Z., O.J.Y. and Q.X. led the animal studies and immune-cell profiling. L.S. led the HR2 design and, with S.G.B., carried out the neutralization studies. M.W.K. and A.R. fabricating the protein vaccine, and, with Y.Z., tested it via organ-on-a-chip. L.D.W., C.A.H. and G.D.T. quantified IgG against SARS-CoV-2 variants in LN organ-on-a-chip outflows using MSD. T.G. and Z.S. quantified relative anti-spike IgG levels in plasma samples using SiMoA. O.J.Y. and Q.X. drafted the manuscript with the guidance of Y.C.Z. and L.S. and with support by M.W.K. and A.R. in figure and writing preparation. Y.C.Z., O.J.Y., Q.X., L.S., M.W.K., S.G.B., H.D., G.I., T.G., Z.S., S.H.S., A.R., A.J., Y.Z., L.D.W. and C.A.H. performed experiments. O.J.Y. and Q.X. modelled the SQB and peptide/protein-conjugated SQB in fusion with C.M.W. providing assistance. A.R.G., A.V., M.S. and S.B. assisted with the animal study design, model set-up and sampling. J.H.R. and I.C.K. supported the project and manuscript editing. W.M.S., Y.C.Z., D.E.I., G.G. and G.D.T. provided overall guidance for the project and edited the manuscript.

Competing interests

W.M.S., J.H.R. and Y.C.Z. are inventors on US patent application PCT/US2020/036281 filed on 5 June 2020 by the Dana-Farber Cancer Institute, Korea Institute of Science & Technology and Wyss Institute, based on this work. Y.C.Z., W.M.S., J.H.R. and I.C.K. are the cofounders of a company called DoriNano, Inc., to translate the DoriVac technology. All other authors declare no competing interests.

Additional information

Supplementary information The online version contains supplementary material available at https://doi.org/10.1038/s41551-026-01614-w.

Correspondence and requests for materials should be addressed to Yang C. Zeng, Girija Goyal, Donald E. Ingber or William M. Shih.

Peer review information *Nature Biomedical Engineering* thanks Hao Pei, Remi Veneziano and the other, anonymous, reviewer(s) for their contribution to the peer review of this work.

[1]Department of Cancer Biology, Dana-Farber Cancer Institute, Harvard Medical School, Boston, MA, USA. [2]Wyss Institute for Biologically Inspired Engineering, Harvard University, Boston, MA, USA. [3]Department of Biological Chemistry and Molecular Pharmacology, Harvard Medical School, Boston, MA, USA. [4]Harvard-Massachusetts Institute of Technology (MIT) Division of Health Sciences and Technology, Massachusetts Institute of Technology, Cambridge, MA, USA. [5]Department of Systems Biology, Harvard Medical School, Boston, MA, USA. [6]Department of Pathology, Brigham and Women's Hospital, Harvard Medical School, Boston, MA, USA. [7]Medicinal Materials Research Center, Biomedical Research Institute, Korea Institute of Science and Technology (KIST), Seoul, Republic of Korea. [8]Center for Human Systems Immunology, Departments of Surgery and Integrative Immunobiology, Duke University School of Medicine, Durham, NC, USA. [9]KU-KIST Graduate School of Converging Science and Technology, Korea University, Seoul, Republic of Korea. [10]Vascular Biology Program, Department of Surgery, Boston Children's Hospital and Harvard Medical School, Boston, MA, USA. [11]Harvard John A. Paulson School of Engineering and Applied Sciences, Boston, MA, USA. [12]These authors contributed equally: Yang C. Zeng, Olivia J. Young, Qiancheng Xiong, Longlong Si, Min Wen Ku. ✉e-mail: yang_zeng@dfci.harvard.edu; girija.goyal@wyss.harvard.edu; don.ingber@wyss.harvard.edu; william_shih@dfci.harvard.edu

nature portfolio

Corresponding author(s): Yang C. Zeng, William M. Shih, Donald E. Ingber, Girija Goyal

Last updated by author(s): Nov 27, 2025

Reporting Summary

Nature Portfolio wishes to improve the reproducibility of the work that we publish. This form provides structure for consistency and transparency in reporting. For further information on Nature Portfolio policies, see our Editorial Policies and the Editorial Policy Checklist.

Statistics

For all statistical analyses, confirm that the following items are present in the figure legend, table legend, main text, or Methods section.

n/a	Confirmed	
☐	☒	The exact sample size (*n*) for each experimental group/condition, given as a discrete number and unit of measurement
☐	☒	A statement on whether measurements were taken from distinct samples or whether the same sample was measured repeatedly
☐	☒	The statistical test(s) used AND whether they are one- or two-sided *Only common tests should be described solely by name; describe more complex techniques in the Methods section.*
☒	☐	A description of all covariates tested
☐	☒	A description of any assumptions or corrections, such as tests of normality and adjustment for multiple comparisons
☐	☒	A full description of the statistical parameters including central tendency (e.g. means) or other basic estimates (e.g. regression coefficient) AND variation (e.g. standard deviation) or associated estimates of uncertainty (e.g. confidence intervals)
☐	☒	For null hypothesis testing, the test statistic (e.g. *F*, *t*, *r*) with confidence intervals, effect sizes, degrees of freedom and *P* value noted *Give P values as exact values whenever suitable.*
☒	☐	For Bayesian analysis, information on the choice of priors and Markov chain Monte Carlo settings
☒	☐	For hierarchical and complex designs, identification of the appropriate level for tests and full reporting of outcomes
☒	☐	Estimates of effect sizes (e.g. Cohen's *d*, Pearson's *r*), indicating how they were calculated

Our web collection on statistics for biologists contains articles on many of the points above.

Software and code

Policy information about availability of computer code

Data collection	Typhoon, Sapphire imaging, Gel Doc EZ Imager (Bio-Rad), TEM, AMT Image Capture Engine Software, flow cytometry machine CytoFlex LX, Biotek NEO 2 microplate reader, ELIspot plate reader, HD-X Analyzer (Quanterix), Bio-Plex 3D Suspension Array System, NanoDrop, MSD Meso Sector S 600MM plate reader
Data analysis	Graphpad Prism (v10) was used for plotting and statistical analysis. FlowJo (v10.10.0) was used for analysis of FACS data. Fiji (ImageJ v1.53) was used for image analysis. MSD Discovery Workbench 4.0 was used to analyze organ-on-a-chip data. Microsoft office for Mac version 16.80 was used to draft the manuscript (Excel, Word, and Powerpoint).

For manuscripts utilizing custom algorithms or software that are central to the research but not yet described in published literature, software must be made available to editors and reviewers. We strongly encourage code deposition in a community repository (e.g. GitHub). See the Nature Portfolio guidelines for submitting code & software for further information.

Data

Policy information about availability of data

All manuscripts must include a data availability statement. This statement should provide the following information, where applicable:

- Accession codes, unique identifiers, or web links for publicly available datasets
- A description of any restrictions on data availability
- For clinical datasets or third party data, please ensure that the statement adheres to our policy

Data supporting the findings of this study are presented in the paper and the supplementary materials. Source data for the figures will be provided with this paper.

Research involving human participants, their data, or biological material

Policy information about studies with human participants or human data. See also policy information about sex, gender (identity/presentation), and sexual orientation and race, ethnicity and racism.

Reporting on sex and gender	Not applicable; tissues were obtained from an institutional biobank.
Reporting on race, ethnicity, or other socially relevant groupings	Not applicable; tissues were obtained from an institutional biobank.
Population characteristics	Not applicable; tissues were obtained from an institutional biobank.
Recruitment	Not applicable; tissues were obtained from an institutional biobank.
Ethics oversight	Tissues were obtained from the Crimson Biomaterials Collection Core Facility under approval of Harvard University's Institutional Review Board.

Note that full information on the approval of the study protocol must also be provided in the manuscript.

Field-specific reporting

Please select the one below that is the best fit for your research. If you are not sure, read the appropriate sections before making your selection.

☒ Life sciences ☐ Behavioural & social sciences ☐ Ecological, evolutionary & environmental sciences

For a reference copy of the document with all sections, see nature.com/documents/nr-reporting-summary-flat.pdf

Life sciences study design

All studies must disclose on these points even when the disclosure is negative.

Sample size	Sample sizes were predetermined from past and/or small pillot experiments, to obtain statistically significant results. For animal studies, 8 mice were applied per group. For intramuscular longitudinal studies, 4 mice were used as controls and 2 mice were used for each treatment group. For in vitro studies, a minimum of three replicates was applied in most cases, unless we were limited by the amount of patient or mouse sample.
Data exclusions	No mice were excluded from the study.
Replication	Mouse studies were performed with the reported biological replicates. All other experiments were performed once for each time point with at the reported biological replicates in the figure captions.
Randomization	All mice were randomly divided into multiple groups. For pseudovirus studies, randomization is not relevant, because most studies were performed with predefined cell lines. Organ-on-a-chip studies were performed with patient samples and the treatment was randomized with respect to the patient samples.
Blinding	Blinding was done for SiMoA; each sample was relabeled with non-descript numbers. No blinding was done for other experiments.

Reporting for specific materials, systems and methods

We require information from authors about some types of materials, experimental systems and methods used in many studies. Here, indicate whether each material, system or method listed is relevant to your study. If you are not sure if a list item applies to your research, read the appropriate section before selecting a response.

Materials & experimental systems

n/a	Involved in the study
☐	☒ Antibodies
☐	☒ Eukaryotic cell lines
☒	☐ Palaeontology and archaeology
☐	☒ Animals and other organisms
☒	☐ Clinical data
☒	☐ Dual use research of concern
☒	☐ Plants

Methods

n/a	Involved in the study
☒	☐ ChIP-seq
☐	☒ Flow cytometry
☒	☐ MRI-based neuroimaging

Antibodies

Antibodies used

Antibodies, along with the supplier name and catalog number, are detailed in Supplementary Tables 4-6, 11-12, and 18 in the supplemental materials.

Validation

The catalog numbers we provided can source to the detailed information of the antibodies including validations at the supplier's website (see links below). The antibodies, as listed in Supplementary Tables 4-6, 11-12, and 18, mostly have a host species of rat (for mouse antibodies) and mouse (for human antibodies) and reactivity with mouse and/or human, depending on the experiment. These antibodies were used for flow cytometry analysis.

All primary antibodies were used without additional validation. The validation of all the antibodies could be found from the corresponding supplier as listed below:

- Brilliant Violent 510 anti-mouse CD11c (Catalog #117338): https://www.biolegend.com/en-gb/products/brilliant-violet-510-anti-mouse-cd11c-antibody-8491
- PE anti-mouse CD40 (Catalog #124610): https://www.biolegend.com/en-gb/products/pe-anti-mouse-cd40-antibody-4983
- APC/Fire™ 750 anti-mouse CD80 (Catalog #104740): https://www.biolegend.com/en-gb/products/apc-fire-750-anti-mouse-cd80-antibody-14403
- PE/Cyanine7 anti-mouse CD86 (Catalog #105014): https://www.biolegend.com/en-gb/products/pe-cyanine7-anti-mouse-cd86-antibody-3046
- Brilliant Violet 421™ anti-mouse I-A/I-E (MHC-II) (Catalog #107632): https://www.biolegend.com/en-gb/products/brilliant-violet-421-anti-mouse-i-a-i-e-antibody-7147
- Brilliant Violet 785™ anti-mouse CD274 (B7-H1, PD-L1) (Catalog #124331): https://www.biolegend.com/en-gb/products/brilliant-violet-785-anti-mouse-cd274-b7-h1-pd-l1-antibody-13497
- PerCP/Cyanine5.5 anti-mouse CD205 (DEC-205) (Catalog #138207): https://www.biolegend.com/en-gb/products/percp-cyanine5-5-anti-mouse-cd205-dec-205-antibody-6728
- Brilliant Violet 605™ anti-mouse/human CD11b (Catalog #101257): https://www.biolegend.com/en-gb/products/brilliant-violet-605-anti-mouse-human-cd11b-antibody-7637
- Alexa Fluor® 700 anti-mouse CD103 (Catalog #121442): https://www.biolegend.com/en-gb/products/alexa-fluor-700-anti-mouse-cd103-antibody-17970
- FITC anti-mouse Ly-6G/Ly-6C (Gr-1) (Catalog #108406): https://www.biolegend.com/en-gb/products/fitc-anti-mouse-ly-6g-ly-6c-gr-1-antibody-458
- Zombie UV Fixable Viability Kit (Catalog #423108): https://www.biolegend.com/en-us/products/zombie-uv-fixable-viability-kit-9336
- Brilliant Violet 510™ anti-mouse/human CD45R/B220 (Catalog #103247): https://www.biolegend.com/en-gb/products/brilliant-violet-510-anti-mouse-human-cd45r-b220-antibody-7996
- Alexa Fluor® 700 anti-mouse CD19 (Catalog #115528): https://www.biolegend.com/en-gb/products/alexa-fluor-700-anti-mouse-cd19-antibody-3391
- Brilliant Violet 650™ anti-mouse CD138 (Syndecan-1) (Catalog #142518): https://www.biolegend.com/en-gb/products/brilliant-violet-650-anti-mouse-cd138-syndecan-1-antibody-8800
- Brilliant Violet 785™ anti-mouse TER-119/Erythroid Cells (Catalog #116245): https://www.biolegend.com/en-gb/products/brilliant-violet-785-anti-mouse-ter-119-erythroid-cells-antibody-14206
- PE/Fire™ 700 anti-mouse CD38 (Catalog #102747): https://www.biolegend.com/en-gb/products/pe-fire-700-anti-mouse-cd38-antibody-20721
- PerCP/Cyanine5.5 anti-mouse IgG1 (Catalog #406612): https://www.biolegend.com/en-gb/products/percp-cyanine5-5-anti-mouse-igg1-8488
- Brilliant Violet 421™ anti-mouse IgG2a (Catalog #407117): https://www.biolegend.com/en-gb/products/brilliant-violet-421-anti-mouse-igg2a-antibody-14633
- PE/Cyanine7 anti-mouse CD40 (Catalog #124622): https://www.biolegend.com/en-gb/products/pe-cyanine7-anti-mouse-cd40-antibody-7165
- APC/Fire™ 750 anti-mouse/rat/human CD27 (Catalog #124237): https://www.biolegend.com/en-gb/products/apcfire-750-anti-mouserathuman-cd27-antibody-17644
- PE/Dazzle™ 594 anti-mouse CD273 (B7-DC, PD-L2) (Catalog #107216): https://www.biolegend.com/en-gb/products/pedazzle594-anti-mouse-cd273-antibody-15630
- FITC anti-mouse CD95 (Fas) (Catalog #152606): https://www.biolegend.com/en-gb/products/fitc-anti-mouse-cd95-fas-antibody-13897
- Brilliant Violet 785™ anti-mouse CD3 (Catalog #100232): https://www.biolegend.com/en-gb/products/brilliant-violet-785-anti-mouse-cd3-antibody-7953
- APC/Cyanine7 anti-mouse CD8a (Catalog #100713): https://www.biolegend.com/en-gb/products/apc-cyanine7-anti-mouse-cd8a-antibody-2269
- PE anti-mouse CD4 (Catalog #100408): https://www.biolegend.com/en-gb/products/pe-anti-mouse-cd4-antibody-250

- PE/Cyanine7 anti-mouse CD69 (Catalog #104512): https://www.biolegend.com/en-gb/products/pe-cyanine7-anti-mouse-cd69-antibody-3168
- PerCP anti-mouse CD62L (Catalog #104430): https://www.biolegend.com/en-gb/products/percp-anti-mouse-cd62l-antibody-4273
- Alexa Fluor® 700 anti-mouse/human CD44 (Catalog #103026): https://www.biolegend.com/en-gb/products/alexa-fluor-700-anti-mouse-human-cd44-antibody-3406
- APC anti-mouse CD127 (IL-7Rα) (Catalog #135012): https://www.biolegend.com/en-gb/products/apc-anti-mouse-cd127-il-7ralpha-antibody-6191
- Brilliant Violet 650™ anti-mouse CD25 (Catalog #102037): https://www.biolegend.com/en-gb/products/brilliant-violet-650-anti-mouse-cd25-antibody-7640
- Brilliant Violet 605™ anti-mouse CD279 (PD-1) (Catalog #135220): https://www.biolegend.com/en-gb/products/brilliant-violet-605-anti-mouse-cd279-pd-1-antibody-7648
- Alexa Fluor® 488 anti-mouse CD107a (LAMP-1) (Catalog #121608): https://www.biolegend.com/en-gb/products/alexa-fluor-488-anti-mouse-cd107a-lamp-1-antibody-3588
- Brilliant Violet 421™ anti-mouse FOXP3 (Catalog #126419): https://www.biolegend.com/en-gb/products/brilliant-violet-421-anti-mouse-foxp3-antibody-12143
- PE/Dazzle™ 594 anti-mouse TNF-α (Catalog #506346): https://www.biolegend.com/en-gb/products/pe-dazzle-594-anti-mouse-tnf-alpha-antibody-12118
- PE/Cyanine5 anti-mouse IL-2 (Catalog #503824): https://www.biolegend.com/en-gb/products/pe-cyanine5-anti-mouse-il-2-antibody-5501
- Brilliant Violet 510™ anti-mouse IFN-γ (Catalog #505841): https://www.biolegend.com/en-gb/products/brilliant-violet-510-anti-mouse-ifn-gamma-antibody-8610
- Brilliant Violet 421™ anti-human CD1c (Catalog #331526): https://www.biolegend.com/en-gb/products/brilliant-violet-421-anti-human-cd1c-antibody-7260
- BD Horizon™ BUV395 Mouse Anti-Human CD14 (Catalog #563561): https://www.bdbiosciences.com/en-eu/products/reagents/flow-cytometry-reagents/research-reagents/single-color-antibodies-ruo/buv395-mouse-anti-human-cd14.563561
- Brilliant Violet 605™ anti-human CD86 (Catalog #305430): https://www.biolegend.com/en-gb/products/brilliant-violet-605-anti-human-cd86-antibody-7805
- APC/Fire™ 750 anti-human CD40 (Catalog #334345): https://www.biolegend.com/en-gb/products/apc-fire-750-anti-human-cd40-antibody-15972
- PE/Cyanine7 anti-human HLA-DR (Catalog #307616): https://www.biolegend.com/en-gb/products/pe-cyanine7-anti-human-hla-dr-antibody-2862
- FITC anti-human CD83 (Catalog #305306): https://www.biolegend.com/en-gb/products/fitc-anti-human-cd83-antibody-680
- ViaKrome 808 Fixable Viability Dye (Catalog #C36628): https://www.beckman.com/reagents/coulter-flow-cytometry/cell-health-research-assays/viakrome-fixable-viability-dyes/c36628
- PerCP/Cyanine5.5 anti-human CD3 (Catalog #317336): https://www.biolegend.com/en-gb/products/percp-cyanine5-5-anti-human-cd3-antibody-8220
- Brilliant Violet 650™ anti-human CD4 (Catalog #317436): https://www.biolegend.com/en-gb/products/brilliant-violet-650-anti-human-cd4-antibody-7786
- Alexa Fluor® 700 anti-human CD8 (Catalog #344724): https://www.biolegend.com/en-gb/products/alexa-fluor-700-anti-human-cd8-antibody-9062
- Brilliant Violet 421™ anti-human IFN-γ (Catalog #506538): https://www.biolegend.com/en-gb/products/brilliant-violet-421-anti-human-ifn-gamma-antibody-17133
- FITC anti-human TNF-α (Catalog #502906): https://www.biolegend.com/en-gb/products/fitc-anti-human-tnf-alpha-antibody-1345
- PE/Cyanine7 anti-human IL-2 (Catalog #500326): https://www.biolegend.com/en-gb/products/pe-cyanine7-anti-human-il-2-antibody-6513
- Brilliant Violet 421™ Mouse IgG1, κ Isotype Ctrl (Catalog #400158): https://www.biolegend.com/en-gb/products/brilliant-violet-421-mouse-igg1-kappa-isotype-ctrl-7194
- FITC Mouse IgG1, κ Isotype Ctrl (Catalog #400108): https://www.biolegend.com/en-gb/products/fitc-mouse-igg1-kappa-isotype-ctrl-1406
- PE/Cyanine7 Rat IgG2a, κ Isotype Ctrl (Catalog #400522): https://www.biolegend.com/en-gb/products/pe-cyanine7-rat-igg2a-kappa-isotype-ctrl-1935
- Brilliant Violet 421™ anti-mouse T-bet (Catalog #644832): https://www.biolegend.com/en-us/products/brilliant-violet-421-anti-t-bet-antibody-7281
- FITC anti-mouse CD64 (FcγRI) (Catalog #139316): https://www.biolegend.com/en-us/products/fitc-anti-mouse-cd64-fcgammari-antibody-12422
- PE anti-mouse NK-1.1 (Catalog #156504): https://www.biolegend.com/en-us/products/pe-anti-mouse-nk-1-1-antibody-16926
- PerCP/Cyanine5.5 anti-mouse CD279 (PD-1) (Catalog #135208): https://www.biolegend.com/en-us/products/percp-cyanine5-5-anti-mouse-cd279-pd-1-antibody-6496

Eukaryotic cell lines

Policy information about cell lines and Sex and Gender in Research

Cell line source(s)	Human ACE2-293 T cells were obtained from Takara Bio (Catalog #631289) and used for the pseudovirus assay. For the lymph-node-on-a-chip and tonsil organoid studies, human patient-derived apheresis collars and tonsil samples were obtained from the Crimson Biomaterials Collection Core Facility under approval of Harvard University's Institutional Review Board.
Authentication	Cell lines were authenticated by the supplier (Takara Bio). After obtaining the cell lines, each cell line was maintained separately and stocked after early passage, minimizing the potential for contamination and the preservation of cell identity. Patient samples did not require authentication.
Mycoplasma contamination	Human ACE2-293 T cells were tested by the manufacterer and confirmed to be free of mycoplasma contamination. Patient-derived cells were obtained from healthy donors, free of infectious disease, and only applied for in vitro culture. As such, patient-derived cells were not tested for mycoplasma contamination.

Commonly misidentified lines (See ICLAC register)	No commonly misidentified cell lines were used.

Animals and other research organisms

Policy information about studies involving animals; ARRIVE guidelines recommended for reporting animal research, and Sex and Gender in Research

Laboratory animals	Female C57BL/6 mice (Jackson Laboratory) at 6-8 weeks were applied for the in vivo studies.
Wild animals	The study did not involve wild animals.
Reporting on sex	Sex-based analysis was not conducted and sex was not considered in the study design.
Field-collected samples	The study did not involve samples collected from the field.
Ethics oversight	All animal studies and procedures were carried out following federal, state and local guidelines, relying on animal protocols approved by the institutional animal care and use committees (IACUC) at Dana Farber Cancer Institute and at Harvard Medical School.

Note that full information on the approval of the study protocol must also be provided in the manuscript.

Plants

Seed stocks	Plants were not used in this study.
Novel plant genotypes	Plants were not used in this study.
Authentication	Plants were not used in this study.

Flow Cytometry

Plots

Confirm that:

☒ The axis labels state the marker and fluorochrome used (e.g. CD4-FITC).

☒ The axis scales are clearly visible. Include numbers along axes only for bottom left plot of group (a 'group' is an analysis of identical markers).

☒ All plots are contour plots with outliers or pseudocolor plots.

☒ A numerical value for number of cells or percentage (with statistics) is provided.

Methodology

Sample preparation	Cell suspensions collected from lymph node, blood, spleens, bone marrow, or harvested from the lymph-node-on-a-chip or tonsil organoid systems were washed with PBS and stained with Zombie UV viability dye (BioLegend, #423108) or ViaKrome 808 Fixable Viability Dye (Beckman Coulter #C36628) and then washed with cell staining buffer (BioLegend, #420201). The cells were then stained with cell surface antibodies conjugated with various fluorophores (Supplementary Tables 4-6, 11-12, 18). Intracellular staining was initiated by fixation and/or permeabilization reagents (BioLegend, #424401). Cells were then stained with antibodies conjugated with various fluorophores. Antibodies (Supplementary Tables 4-6, 11-12, 18) were arranged into different panels, appropriate compensations were set up to compensate for fluorescent emission overlap, and the stained cells were analyzed on a Cytoflex LX. Storage events were gated on the population of interest. Flow data was analyzed using FlowJo (v10.10.0). Detailed cell suspension processing information was included in the methods.
Instrument	CytoFlex LX
Software	CytoFlex were used for collection of data and FlowJo (v10.10.0) was used for analysis. The collected data was plotted and analyzed by GraphPad Prism.
Cell population abundance	No sorting was performed using the flow cytometer. Flow cytometry was only used for the purpose of analysis.
Gating strategy	We employed a standard gating procedure to exclude debris from all cells initially, followed by singlets and live cells. The gating process for identifying single-marker or double-marker positive populations was conducted within the live cell

population or other relevant parental populations. Detailed gating strategies for immune cell profiling could be seem from Supplementary Figure 2, 5, 9, 11, 12, 16, 18, 19.

☒ Tick this box to confirm that a figure exemplifying the gating strategy is provided in the Supplementary Information.